



Constraining Cosmic-Ray Ionization Rates and Chemical Timescales in Massive Hot Cores

Christopher J. Barger^{1,2} and Robin T. Garrod^{1,2}

¹ Department of Chemistry, University of Virginia, Charlottesville, VA 22904-4319, USA; cjb2ck@virginia.edu

² Department of Astronomy, University of Virginia, Charlottesville, VA 22904-4325, USA

Received 2019 February 21; revised 2019 November 18; accepted 2019 November 22; published 2020 January 6

Abstract

Several studies have demonstrated that the cosmic-ray ionization rate is highly variable in the interstellar medium. However, constraints of this rate for several regions, including those that contain hot cores, are lacking. Hot cores are appealing sources to study given their rich chemical complexity. The chemistry of these cores can be influenced by both their cosmic-ray ionization rates and their warm-up timescales; however, understanding the chemical response to these parameters requires further investigation. We study these effects using the astrochemical hot-core modeling code *MAGICKAL*, in which we construct a grid of 81 models using nine ionization rates and nine warm-up timescales. We also simulate local thermodynamic equilibrium radiative transfer for these models to obtain results that can be directly compared with observations. We compare molecular emission of these models with observations toward NGC 6334 IRS 1, NGC 7538 IRS 1, W3(H₂O), and W33A in an effort to constrain their cosmic-ray ionization rates and warm-up timescales. Our best fits to the observations suggest that these sources possess elevated cosmic-ray ionization rates, compared to the canonical value of $1.3 \times 10^{-17} \text{ s}^{-1}$ used in previous modeling studies, and rapid warm-up timescales. We also demonstrate that there exists a strong correlation between the cosmic-ray ionization rate and the total hydrogen column density of a source and a strong correlation between the warm-up timescale and total source mass. Furthermore, these relationships are in good agreement with other theoretical studies.

Unified Astronomy Thesaurus concepts: [Astrochemistry \(75\)](#); [Cosmic rays \(329\)](#); [Line intensities \(2084\)](#); [Chemical abundances \(224\)](#); [Massive stars \(732\)](#)

1. Introduction

Cosmic rays are vital to the evolution of chemical complexity in the interstellar medium (ISM), especially in high-extinction regions that UV photons are unable to penetrate. There are two dominant processes by which cosmic rays affect this chemistry: (i) the direct collisional ionization of atoms and molecules, most notably hydrogen, and (ii) collisional excitation of gas-phase H₂ in particular, to generate Lyman–Werner band photons that can ionize and dissociate other chemical species (Prasad & Tarafdar 1983). Importantly, process (i) leads readily to the production of the ions H₂⁺, H⁺, and He⁺ in the gas phase. H₂⁺ reacts easily with neutral molecular hydrogen to form H₃⁺; this ion drives much of the ion–molecule chemistry in dense interstellar clouds, through proton donation to neutral species, and is responsible for the gas-phase formation of simple molecules including H₂O, NH₃, and CH₄ (Herbst & Millar 2008). The cosmic-ray-induced UV field can also influence the chemical evolution of dust-grain-surface ices, through the photodissociation of major ice constituents such as water, formaldehyde, methanol, ammonia, and methane, to generate radicals including OH, HCO, CH₃, CH₃O, CH₂OH, and NH₂. Under warm conditions in which these radicals become thermally mobile, they may react to form a variety of complex organic molecules (COMs; Garrod & Herbst 2006; Garrod et al. 2008).

The cosmic-ray ionization rate, ζ , is typically defined in chemical models as the rate at which H₂ is ionized, while the rates of ionization and dissociation of other species usually are defined in fixed ratios to this value. For species with an ionization potential or dissociation energy low enough to allow the relevant process to be initiated by the secondary

Lyman–Werner field, and not only by direct cosmic-ray collision, the rates of those processes may be as much as several orders of magnitude greater than the base rate ζ .

Several techniques have been employed to measure the cosmic-ray ionization rate in different regions of the ISM. Measurement of H₃⁺ abundance has been a popular avenue in determining ζ , due to its direct dependence on cosmic-ray ionization of H₂. Oka et al. (2005) used total column density measurements of H₃⁺ to infer a value $\zeta = (2\text{--}7) \times 10^{-15} \text{ s}^{-1}$ toward diffuse regions of the Galactic center. Le Petit et al. (2016) modeled H₃⁺ chemistry in the same regions and calculated ζ to be on the order of 10^{-14} s^{-1} . Other studies have invoked alternative means of determining the cosmic-ray ionization rate elsewhere in the ISM. Van der Tak & van Dishoeck (2000) used CO and HCO⁺ observations and modeling to derive $\zeta = (3 \pm 2) \times 10^{-17} \text{ s}^{-1}$ toward select massive protostars. Van der Tak et al. (2006) mapped H₃O⁺ toward Sgr B2 and calculated $\zeta = 4 \times 10^{-16} \text{ s}^{-1}$. Caselli et al. (1998) used fractional ionization rates of HCO⁺ and DCO⁺ to constrain ζ in the range of 10^{-18} to 10^{-16} s^{-1} . Ceccarelli et al. (2011) and Vaupré et al. (2014) also used measurements of HCO⁺ and DCO⁺ to constrain $\zeta = 10^{-15} \text{ s}^{-1}$ in supernova remnants. Favre et al. (2018) used observations and modeling of c-C₃H₂ toward OMC-2 FIR4 to calculate $\zeta = 4 \times 10^{-14} \text{ s}^{-1}$.

Despite thorough investigation of ζ in these studies, it remains unclear how applicable these results are generally or to other, specific sources, especially for the purposes of understanding chemistry in high-mass star-forming cores (see below). Gaches et al. (2019) suggest that the determination of cosmic-ray ionization rates through the above techniques is

only reliable when cosmic rays dominate source thermochemistry, which may not be the case.

Furthermore, these results and others from related studies (e.g., Webber 1998; Le Petit et al. 2004; Yusef-Zadeh et al. 2013) indicate that ζ varies by several orders of magnitude throughout the Galactic ISM. The variability suggests that assigning to a source a uniform or canonical ionization rate for the purposes of chemical modeling may not be appropriate; unique physical conditions can alter the local ζ within a source, even if ζ is constrained in the surrounding medium. Rimmer et al. (2012) calculated depth-dependent cosmic-ray ionization rates in an interstellar cloud, using a Monte Carlo method to consider attenuation by gas-phase particles and magnetic field-related losses. Padovani et al. (2009) and Padovani & Galli (2011) also used similar approaches, with varying treatments for the magnetic interactions and using different cosmic-ray fluxes from the literature. More recent work by Padovani et al. (2018) looked carefully at the role of the flux low-energy protons in such calculations. Rimmer et al. (2012) calculated ζ for visual extinctions up to 10 mag, while Padovani et al. (2009) obtained values to rather larger extinctions, corresponding to hydrogen column densities $N(\text{H}_2) \leq 10^{25} \text{ cm}^{-2}$. These two studies determined that the ionization rate should fall off as a power law with respect to hydrogen column density, with indices ranging from $a = 0.6$ to 1 (Rimmer et al. 2012) and from 0.4 to 0.8 (Padovani et al. 2009), while Padovani et al. (2018) also found the same general trend. Interstellar clouds or star-forming cores of greater column density should therefore experience lower cosmic-ray ionization rates, in cases where the ambient intercloud rate is otherwise the same. Accordingly, for an accurate understanding of local chemical conditions, ζ should be determined explicitly for a given source. Unfortunately, cosmic-ray ionization rates are poorly constrained by observations for many interstellar regions of chemical interest, including well-known star-forming sources known as hot cores.

Hot cores represent a transient stage of massive star formation that is characterized by strong molecular emission and the presence of a broad range of COMs. The temperatures and densities of these cores are typically greater than 100 K and 10^7 cm^{-3} , respectively (Choudhury et al. 2015). Given their high densities, local thermodynamic equilibrium (LTE) is usually a good approximation for modeling the line emission from the inner regions where most of the complex molecular material resides. COMs detected toward hot cores include alcohols, aldehydes, carboxylic acids, ethers, and esters (Garrod & Widicus Weaver 2013). As such, hot cores are compelling regions of study for detections of new COMs and/or prebiotic species (e.g., Belloche et al. 2014), although molecules of true biological significance, such as amino acids, have not yet been detected (see, e.g., Snyder et al. 2005).

The influence of the specific value of ζ on the chemistry of these rich and diverse regions has been little investigated, and it is unclear what value may be optimal for the production of COMs. The dominant paradigm currently used to explain the production of most COMs in hot cores relies on the cosmic-ray-induced UV photodissociation of simple grain-surface ice species such as methanol, producing radicals that may further react with each other if grain temperatures are high enough to allow them to become mobile (typically >20 K). The addition of radicals in this way thus leads to typically observed COMs like methyl formate (HCOOCH_3) becoming abundant on the

grain surfaces, and which ultimately desorb into the gas phase when the protostar heats its envelope and thus the characteristic hot-core temperatures (>100 K) are achieved. However, the dominant destruction mechanism for gas-phase COMs in most chemical networks involves reaction with simple ions such as H_3^+ , H_3O^+ , and several others, whose abundances are also directly dependent on the cosmic-ray ionization rate. The product molecules formed as the result of photodissociation of smaller species on the grains may also be dissociated by the same means, either in the gas phase or on the grains, prior to thermal desorption. The observable abundances of COMs must therefore be dependent on the balance between cosmic-ray-induced formation and a set of separate but related cosmic-ray-induced destruction mechanisms.

Typical values of ζ used in astrochemical models are on the order of 10^{-17} s^{-1} . Garrod (2013, hereafter G13) and related modeling efforts have consistently used $\zeta = 1.3 \times 10^{-17} \text{ s}^{-1}$, following estimates for dark clouds (Duley & Williams 1993), while others have adopted a broader range of values; Shingledecker et al. (2018) modeled cold-core ice chemistry using values from 10^{-17} to 10^{-14} s^{-1} . Although some authors have recognized the necessity to consider ζ as a free parameter in hot-core models (Allen et al. 2018), there persists a lack of information about how molecular abundances trend with varying ζ in the gas and solid phases for hot cores. The picture is further complicated by the fact that the timescale for the exposure of both grain-surface and gas-phase species to CR-induced processing is also poorly constrained, especially during the important period at elevated temperatures when reactive radicals on the dust grains become mobile enough to produce COMs. The time taken for the temperature of the hot core to progress from cold-core values around 10 K to the characteristic hot-core temperature, i.e., the “warm-up” timescale, t_{wu} , has been often been assigned a range of values; Garrod & Herbst (2006) adopted three timescales ranging from $t_{\text{wu}} = 5 \times 10^4$ to 10^6 yr, corresponding to a temperature progression from 10 to 200 K, following the approach of Viti & Williams (1999). Subsequent gas-grain hot-core models have adopted a similar scheme. Values on the shorter end of this range have typically been found to reproduce observational fractional abundances the best (e.g., Belloche et al. 2009). However, this determination has usually been made for models with fixed cosmic-ray ionization rate; ζ and t_{wu} may indeed share a degenerate effect on the chemistry, making the cosmic-ray fluence (i.e., the product ζt_{wu}) perhaps more meaningful than ζ itself.

Using the astrochemical kinetics code *MAGICCAL*, we study the effects of t_{wu} and ζ on the chemistry of hot cores using a grid of generic models run at various cosmic-ray fluences. We concentrate especially on COMs, with the goal of using their observed abundances in specific sources to constrain both t_{wu} and ζ appropriate to those sources. The particular prevalence of COMs in the dense centers of hot cores makes them good candidates to determine ζ specifically in those dense regions.

Past modeling studies of hot-core chemistry have typically used a comparison between modeled fractional abundances and observationally determined values (based on column density ratios) to determine the quality of the match between model and observational data. However, such methods ignore the spatial variation of molecular emission as a function of density, temperature, and fractional abundance, all of which may vary between sources. Determinations of column densities for

particular molecules are also prone to error, especially with single-dish instruments, due to beam dilution. The spatial extents of individual species are likely to depend strongly on the local temperature, as attested by the wide range of excitation temperatures observed for different COMs, even toward the same source. This may be caused by differences in the binding energies of different species, or by the sensitivity of their chemical formation and destruction routes to thermal activation, or by the presence or absence of other species with which they may react under such conditions.

In order to take account of these effects in our comparison between models and observational data, we simulate explicitly the emission from a complement of COMs, using chemical abundance data from the generic model grid mapped onto observationally determined physical profiles for specific sources (van der Tak et al. 2000). The resultant integrated line intensities are then compared with observational values from the molecular line surveys of Bisschop et al. (2007, hereafter B07), following the same approach as G13. We assess the chemistry of the 13 molecules in the B07 survey, as well as glycine, and compare results for four hot-core sources studied by both van der Tak et al. and B07: NGC 6334 IRS 1, NGC 7538 IRS 1, W3(H₂O), and W33A. This analysis allows the best-fitting values of ζ and t_{wu} to be determined for each source.

Details of the specific methods used in this study are provided in Section 2. Analysis of the model results for individual chemical species is presented in Section 3, and the comparison with specific observational sources is given in Section 4. Discussion and conclusions follow in Sections 5 and 6.

2. Methods

To study the effects of the warm-up timescale, t_{wu} , and the cosmic-ray ionization rate, ζ , on the chemistry of hot cores, we implement the three-phase astrochemical modeling code *MAGICKAL*, outlined by G13. *MAGICKAL* integrates the time-dependent gas-phase, grain-surface, and ice-mantle fractional abundances by solving a system of rate equations. The essential details of this model are provided below. In order to compare the chemical results to specific observations in a meaningful way, spectral simulations are conducted, under LTE conditions, using chemical abundances from the models mapped onto spherically symmetric physical profiles for specific sources taken from the literature. The details of this treatment are provided in Section 2.2.

2.1. Chemical Model: *MAGICKAL*

The chemical model employs a three-phase treatment conceived by Hasegawa & Herbst (1993) and further described by Garrod & Pauly (2011). The model uses the chemical network of G13, which includes gas-phase, grain-surface, and ice-mantle reactions. Although more recent work has been done in the laboratory for certain chemical systems relevant to COMs, the G13 model and network are self-consistent and have been tested extensively. The chemistry of methanol (CH₃OH) is considered to be of particular importance to the production of complex organics (e.g., Öberg et al. 2009a), and some laboratory studies have obtained values for important parameters for that system (e.g., Rimola et al. 2014; Álvarez-Barcia et al. 2018). However, in the case of, e.g., Rimola et al.

(2014), the analysis does not consider all of the reactions included in our network for the methanol system (i.e., H-abstraction reactions). For reasons of self-consistency, we retain the reaction barrier treatment for the hydrogenation of CO and H₂CO and abstraction from various species in the methanol system used by G13, which is based on private communications of quantum rate calculations by F. Goumans and S. Andersson, bypassing the need for more basic thermal or tunneling calculations in the G13 code using activation barrier and width estimates.

In our model, surface species may be returned to the gas phase by thermal desorption, reactive desorption, or photo-desorption; the yields for the latter are based on values provided by Öberg et al. (2009b, 2009c), with rates dependent on both the external and cosmic-ray-induced UV fields. Likewise, photodissociation of molecules may be induced by either field but is allowed to occur in all chemical phases. Ivlev et al. (2015) used a new approach for cosmic-ray impacts of individual dust grains; however, the process is stochastic in nature and not readily compatible with our own work. Alternatively, Shingledecker et al. (2017) presented a new model for cosmic-ray interactions in solids; however, its accuracy remains unclear, and so incorporating this work into our model is not currently appropriate. The reactive desorption mechanism assumes an efficiency coefficient $a = 0.01$ (see Garrod et al. 2007), which yields desorption probabilities somewhat less than 1%. During the hot phase, thermal desorption is the dominant desorption process.

Several experiments demonstrate that chemical reactions occurring on interstellar dust grains are important to the production of COMs (e.g., Öberg et al. 2009a; Butscher et al. 2016), and as such, grain chemistry is an important facet of our model. Barrier-mediated thermal diffusion rates determine the reaction rates of surface and bulk species; the diffusional coupling between these two phases is determined by bulk diffusion rates. For surface and bulk-ice reactions with activation energy barriers, reaction rates are based on the faster of the thermal reaction rate and the rate of tunneling through a rectangular barrier; the majority of rates are dominated by the tunneling contribution at the temperatures considered in these models. For activated reactions, simple competition between reaction and thermal diffusion of the reactants is calculated, to determine the overall efficiency of reaction per meeting of the reactants. For the surface chemistry only, the modified-rate approach introduced by Garrod (2008) is used to approximate the stochastic behavior of surface reactants, where applicable. Chemical pathways for glycine and similar species (i.e., glycinol, propionaldehyde, and propionic acid) were incorporated into the chemical network by G13, adopting formation mechanisms consistent with the radical reaction scheme used for other COMs.

2.1.1. Physical Considerations

The physical evolution of the hot core is treated as a two-stage process, following Garrod & Herbst (2006), whose approach was based on that of Viti & Williams (1999). Stage 1 involves the freefall collapse of material of initial gas density $n_{\text{H}} = 3.0 \times 10^3 \text{ cm}^{-3}$, increasing over a period of around 1 Myr to $n_{\text{H}} = 2.0 \times 10^8 \text{ cm}^{-3}$ following Belloche et al. (2014). The visual extinction takes an initial value of 2 and scales with $n_{\text{H}}^{2/3}$. The gas temperature is held at a constant 10 K, whereas the dust temperature is allowed to fall as a

Table 1
Cosmic-Ray Fluence Grid Parameters

Warm-up Timescale		Cosmic-Ray Ionization Rate	
Notation	Time to Reach 200 K (yr)	Notation	$\zeta(\text{s}^{-1})$
t_1	3.13×10^3	ζ_1	2.60×10^{-18}
t_2	6.25×10^3	ζ_2	5.81×10^{-18}
t_3	1.25×10^4	ζ_3^a	1.30×10^{-17}
t_4	2.50×10^4	ζ_4	2.60×10^{-17}
t_5^a	5.00×10^4	ζ_5	5.20×10^{-17}
t_6	1.00×10^5	ζ_6	1.04×10^{-16}
t_7^a	2.00×10^5	ζ_7	2.08×10^{-16}
t_8	4.50×10^5	ζ_8	4.16×10^{-16}
t_9^a	1.00×10^6	ζ_9	8.32×10^{-16}

Note.

^a Original parameters from G13.

function of the visual extinction (see Garrod & Pauly 2011) from 16 to 8 K. The chemistry of stage 1 begins in an entirely atomic state, save for H_2 ; initial chemical abundances are those used by G13.

During stage 2 (warm-up), the dust temperature increases from 8 to 400 K, at a fixed gas density determined at the end of stage 1. Gas and dust temperatures are assumed to be well coupled owing to the high density; thus, the gas is allowed to take on the temperature of the grains as it rises to values above 10 K. Following Garrod & Herbst (2006), G13 adopted three values of the warm-up timescale: $t_{\text{wu}} = 5 \times 10^4$, 2×10^5 , and 10^6 yr. These characteristic timescales correspond to the progression from 8 to 200 K; G13 simply extended the temperature progression to 400 K. To these three possible warm-up timescales, a further six are added in this work (see Section 2.1.2).

Although in the single-point models employed here the temperature varies over time, in the spectral simulations the temperature is treated also as a proxy for the radial dependence of the chemistry. Thus, the more central regions of a hot core have progressed for a longer period of chemical and thermal evolution. This method avoids having to run multiple individual trajectories for each set of physical conditions, allowing the grid of generic models presented here to be applied to multiple observed sources. This approach also implicitly assumes that the thermal history of each parcel of gas in the radial distribution is dominated by its radial position and not, for example, the changing luminosity of a protostellar source. We leave such considerations to future modeling efforts.

2.1.2. Cosmic-Ray Fluence Grid

To allow an investigation of the dependence of hot-core chemistry on the cosmic-ray ionization rate and warm-up timescale, a 9×9 grid of models in t_{wu} and ζ is constructed (Table 1). Each such model begins with an identical stage 1 collapse. The total cosmic-ray fluence in each model during the warm-up period (as defined by the time to reach 200 K) is the product of t_{wu} (s) and ζ (s^{-1}), which we simply quote throughout as a unitless quantity.

The grid consists of nine values of ζ and t_{wu} and incorporates the *large*, *medium*, and *small* values of t_{wu} (t_9 , t_7 , and t_5 respectively) used by G13 and others. Two intermediate t_{wu} (t_8 and t_6) are created and assigned values such that they are

evenly spaced (logarithmically) among the originals. Four smaller t_{wu} ($t_4 - t_1$) are chosen, each of which is a factor of 2 shorter than the last.

Values of ζ are chosen to produce a degeneracy in the cosmic-ray fluence of the models running along the grid's lower left to top right diagonal (Table 2). The diagonal model of t_7 is assigned a standard value of $\zeta_3 = 1.3 \times 10^{-17} \text{ s}^{-1}$ used by G13 and previous versions. The cosmic-ray fluence of this model equals $8.2 \times 10^{-5} \text{ yr s}^{-1}$, and the ζ values for the on-diagonal models of other t_{wu} are chosen to be degenerate with this fluence, producing a set of values ranging from $\zeta = 2.60 \times 10^{-18} \text{ s}^{-1}$ to $8.32 \times 10^{-16} \text{ s}^{-1}$. Since the spacing between the original three t_{wu} is not precisely uniform, the grid is asymmetric and not all diagonals (except the principal diagonal) have the same fluence across each model. Timescales t_8 and t_9 are irregular, as are the ionization rates ζ_1 and ζ_2 .

2.2. Spectral Modeling

The submillimeter spectral line survey of B07 provided integrated intensities for spectral lines in emission from 13 different molecules, for seven high-mass protostellar sources, with data obtained using the James Clerk Maxwell Telescope (JCMT) and the IRAM 30 m telescope. The survey identified typically dozens of lines from each molecule, making this a rich data set for comparison with chemical models. In order to compare our results with the observations of B07 in a direct way, radiative transfer for each molecule detected in that survey is simulated using fractional abundance data from the chemical models, according to the method described by G13. This treatment requires information on the spatially dependent physical conditions within the source being modeled. Spherically symmetric temperature and density profiles for a selection of high-mass sources were fit by van der Tak et al. (2000), four of which were also included in the B07 study: NGC 6334 IRS 1, NGC 7538 IRS 1, W3(H_2O), and W33A. These four sources are thus the target of the spectral calculations.

For each individual simulation of one of the four sources, all temperature-dependent fractional abundance data from one of the models presented in Section 3 are mapped to the corresponding temperature in the profile of that source. This results in a spherically symmetric model of the source, in which the abundance of each molecule in the chemical models is defined, and for which the local emission and absorption coefficients can be calculated. Under the assumption of LTE, plane-parallel radiative transfer is calculated for lines of sight through the source, providing raw emission maps in the plane of the sky for each frequency channel. Spectroscopic information for the calculation of the absorption and emission coefficients relating to each molecule is obtained from the Cologne Database for Molecular Spectroscopy³ and from the JPL molecular spectroscopy database.⁴

Following the radiative transfer calculations, the emission maps are convolved with a Gaussian beam at the on-source position. The beamwidth is frequency dependent and corresponds to the telescope used for the simulation, which is either the JCMT or IRAM 30 m, depending on which instrument was used to obtain which line in the B07 survey. The individually simulated and convolved frequency channels are then used to construct simulated spectra for each observed line. The lines

³ <https://cdms.astro.uni-koeln.de>

⁴ <https://spec.jpl.nasa.gov/>

Table 2
Cosmic-Ray Fluences Corresponding to Each Model

	ζ_1	ζ_2	ζ_3^a	ζ_4	ζ_5	ζ_6	ζ_7	ζ_8	ζ_9
t_1	2.6(−7)	5.3(−7)	1.3(−6)	2.6(−6)	5.1(−6)	1.0(−5)	2.0(−5)	4.1(−5)	8.2(−5)
t_2	5.1(−7)	1.1(−6)	2.6(−6)	5.1(−6)	1.0(−5)	2.0(−5)	4.1(−5)	8.2(−5)	1.6(−4)
t_3	1.0(−6)	2.3(−6)	5.1(−6)	1.0(−5)	2.0(−5)	4.1(−5)	8.2(−5)	1.6(−4)	3.3(−4)
t_4	2.0(−6)	4.6(−6)	1.0(−5)	2.0(−5)	4.1(−5)	8.2(−5)	1.6(−4)	3.3(−4)	6.6(−4)
t_5^a	4.1(−6)	9.2(−6)	2.0(−5)	4.1(−5)	8.2(−5)	1.6(−4)	3.3(−4)	6.6(−4)	1.3(−3)
t_6	8.2(−6)	1.8(−5)	4.1(−5)	8.2(−5)	1.6(−4)	3.3(−4)	6.6(−4)	1.3(−3)	2.6(−3)
t_7^a	1.6(−5)	3.7(−5)	8.2(−5)	1.6(−4)	3.3(−4)	6.6(−4)	1.3(−3)	2.6(−3)	5.2(−3)
t_8	3.7(−5)	8.2(−5)	1.8(−4)	3.7(−4)	7.4(−4)	1.4(−3)	3.0(−3)	5.9(−3)	1.2(−2)
t_9^a	8.2(−5)	1.8(−4)	4.1(−4)	8.2(−4)	1.6(−3)	3.3(−3)	6.6(−3)	1.3(−2)	2.6(−2)

Notes. $a(b) = a \times 10^b$. Values of t_{wu} and ζ are cited using the notation in Table 1. Fluences are given as the product $t_{\text{wu}} \times \zeta$, corresponding to the time required to reach 200 K. The product is unitless, as t_{wu} is converted to seconds.

^a Original parameters from G13.

observed by B07 were generally unblended, but to ensure the same in these simulations, radiative transfer for each line was modeled separately. The resulting spectral emission for each line was then integrated to produce a value directly comparable with the integrated intensities quoted by B07. A frequency resolution of ~ 400 kHz per channel was used in the simulations. Line widths for each source were taken from the average values quoted by B07 and were in the range of $4\text{--}6 \text{ km s}^{-1}$ for the four sources simulated here.

Since we are also interested in the chemistry of glycine and the prospect of its detection in the ISM, we run spectral simulations of it following the same method described here. We use the six lines in ALMA band 6 that were studied by G13. Likewise, each line is modeled separately with the same frequency resolution used for all other simulations. Following G13, we convolve the emission using a beam size of $0''.4$, which is within current ALMA capabilities.

2.3. Population Diagrams

After obtaining line-integrated intensities from the spectroscopic model, we employ the population diagram technique described by Goldsmith & Langer (1999). The integrated intensities are used to derive upper-level populations, which are then plotted as a function of excitation energy to derive total source-averaged molecular column densities (N_{tot}) and excitation temperatures (T_{ex}). If LTE conditions apply and external pumping mechanisms are negligible, excitation temperatures are representative of the kinetic gas temperatures at which molecules emit radiation.

The optical depth, τ , for each frequency channel is calculated explicitly from absorption coefficients in the radiative transfer simulations. Some of the lines of interest in the B07 survey are calculated to have non-negligible optical depths in our simulations. To allow such lines to be used in the population diagrams, a correction factor is applied to their upper-level column densities (N_u). The correction factor is given by Herbst & van Dishoeck (2009) as $C_\tau = \frac{\tau}{1 - e^{-\tau}}$. The value of τ used to determine the correction factor in our simulations is that calculated for the line-center channel.

3. Model Results

The following subsections detail the chemical and physical model results. Chemical mechanisms and fractional abundance trends across the cosmic-ray fluence grid are explored for 14 molecules of interest. These include the 13 detected by B07,

while—to follow up on the study by G13—the results for glycine, the simplest amino acid, are also considered. Analysis of the chemical results includes the use of the population diagram technique to derive source-averaged column densities and excitation temperatures.

3.1. Chemistry

Time- and temperature-dependent fractional abundance plots for pertinent species are provided for selected models from the grid in Figures 1–5. The chemistry of each molecule is briefly recounted in the following subsections, including a description of the main formation and destruction reactions for each. It should be noted that, for the sake of simplicity, only the most influential reactions are discussed. Descriptions of the chemistry are given in the context of the different models with varying t and ζ values; thus, the relative influence of individual mechanisms can vary between the models. The subscript labels (g) and (s) applied to the names of molecules refer to their gas phase and solid phase (i.e., grain surface/mantle), respectively.

In general, molecules may be formed on grains at low temperature by hydrogenation and at somewhat higher temperatures (>20 K) by radical addition. Following their formation, molecules may be destroyed on grains via H-atom abstraction by the surface radicals $\text{OH}_{(s)}$ and $\text{NH}_{2(s)}$ and by cosmic-ray-induced photodissociation (CRPD). Radical–radical and H-addition reactions tend to be more effective as ζ increases, because radicals are produced at greater rates, via CRPD of major grain constituents.

COMs thermally desorb at higher temperatures, typically around 100 K or higher. Large ice abundances do not necessarily translate to large gas abundances, due to the prominence of destruction processes on grains (see Table 3 for a summary of highest and lowest grain and gas-phase abundances). Once released into the gas phase, molecules are typically destroyed through protonation by HCO^+ and H_3O^+ . Once protonated, they recombine with electrons to form a variety of fragments. In the G13 network, the production of a hydrogen atom and a single, stable molecule as the result of electronic recombination of a protonated molecule is assumed to occur in only 5% of cases, where such fractions have not been experimentally determined. Protonation reactions become more efficient as ζ increases, because cosmic-ray ionization increases gas-phase ion and electron abundances (Figure 1).

Thus, the cosmic-ray ionization rate is seen to influence both the formation and destruction of COMs in hot cores.

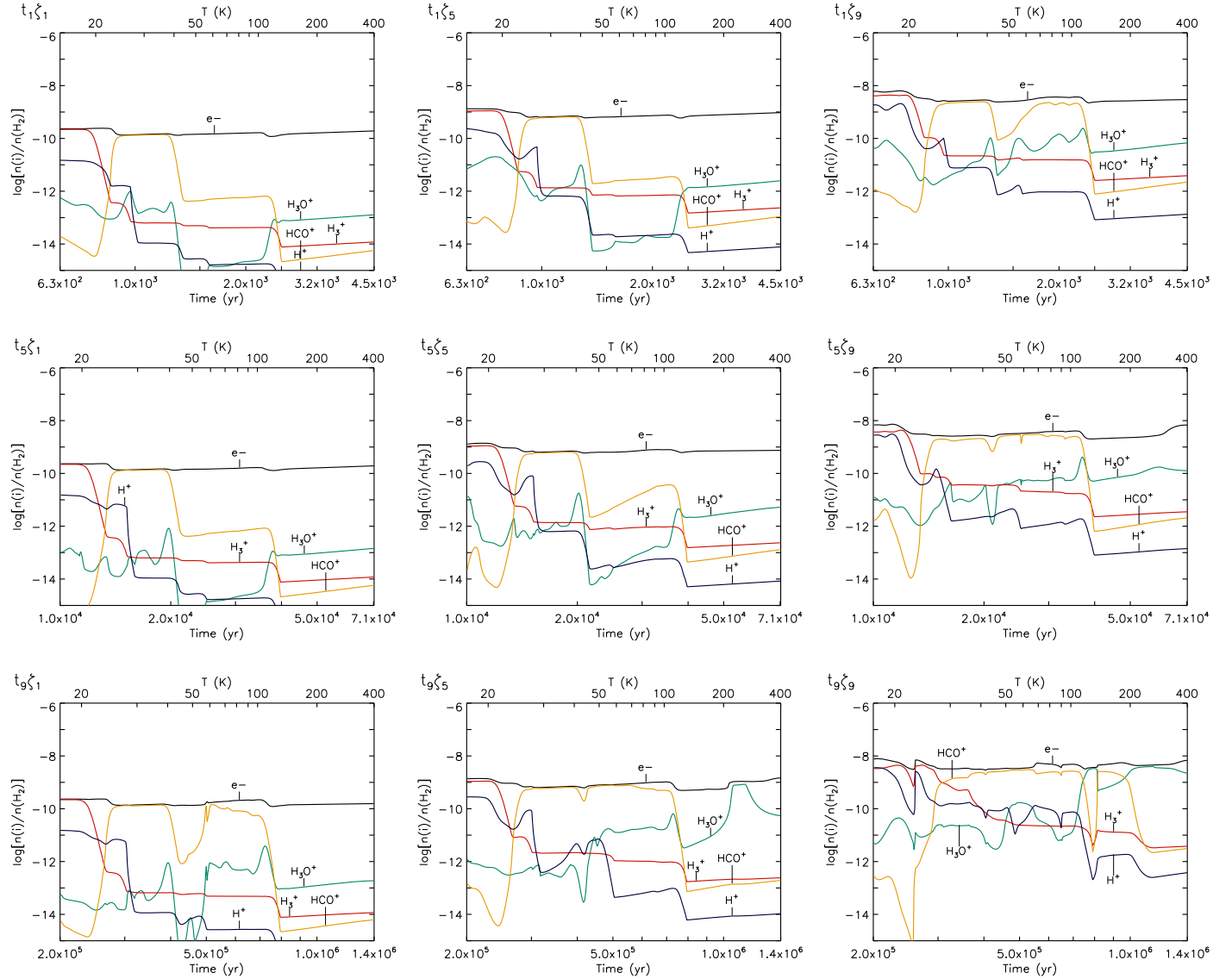


Figure 1. Select time- and temperature-dependent gas-phase fractional abundance plots (with respect to H_2) for electrons and important ions. The fractional abundance, time, and temperature (upper axis) are plotted logarithmically.

Table 3

Highest and Lowest Peak Grain and Gas-phase Fractional Abundances among All Models

Species	Highest (s)	Highest (g)	Lowest (s)	Lowest (g)
CH_3OH	1.0(−5)	1.0(−5)	9.0(−6)	6.0(−11)
H_2CO	2.0(−5)	1.0(−5)	2.0(−6)	3.0(−10)
$HCOOH$	3.0(−7)	8.0(−8)	1.0(−9)	1.0(−11)
CH_3CHO	3.0(−6)	4.0(−7)	6.0(−8)	5.0(−9)
CH_2CO	6.0(−7)	2.0(−7)	2.0(−9)	9.0(−11)
C_3H_4	5.0(−6)	1.0(−7)	5.0(−10)	2.0(−10)
CH_3OCH_3	4.0(−7)	1.0(−7)	6.0(−9)	8.0(−15)
CH_3OCHO	4.0(−7)	2.0(−7)	3.0(−7)	4.0(−14)
C_2H_5OH	5.0(−6)	2.0(−7)	3.0(−8)	2.0(−13)
NH_2CHO	1.0(−6)	1.0(−6)	8.0(−8)	3.0(−13)
$HNCO$	9.0(−8)	6.0(−8)	3.0(−9)	3.0(−11)
CH_3CN	1.0(−7)	6.0(−9)	9.0(−10)	3.0(−10)
C_2H_5CN	1.0(−6)	4.0(−8)	1.0(−8)	1.0(−11)
NH_2CH_2COOH	4.0(−8)	7.0(−10)	3.0(−13)	6.0(−18)

Note. Here (s) refers to solid-phase abundances, and (g) refers to gas-phase abundances.

3.1.1. Methanol

Methanol (CH_3OH) forms on grains during the cold collapse stage, by successive H-atom addition to $CO_{(s)}$. Laboratory studies indicate that this process is efficient at low temperatures (Watanabe & Kouchi 2002; Hidaka et al. 2004). Methanol abundances on the grains remain essentially static in the warm-up prior to desorption in most t_{wu} and ζ models; however, methanol is significantly diminished at 30–40 K for the $t_{wu} = t_9$, $\zeta = \zeta_9$ model (Figure 2, panel $t_9\zeta_9$). This is due to CRPD and to H abstraction by $OH_{(s)}$. These processes are rapid for large ζ , and large t_{wu} values permit them to occur for longer times. CRPD produces $CH_3_{(s)}$, $CH_3O_{(s)}$, and $CH_2OH_{(s)}$ radicals with branching ratios (1/1/5) taken from Öberg et al. (2009a). H abstraction by $OH_{(s)}$ also produces $CH_3O_{(s)}$ and $CH_2OH_{(s)}$. These radicals can be rehydrogenated by atomic H or by radicals capable of donating a hydrogen atom, and they may also donate a hydrogen atom to other reactive species, producing formaldehyde (H_2CO). However, reactions of these with other radicals may also engender formation of other

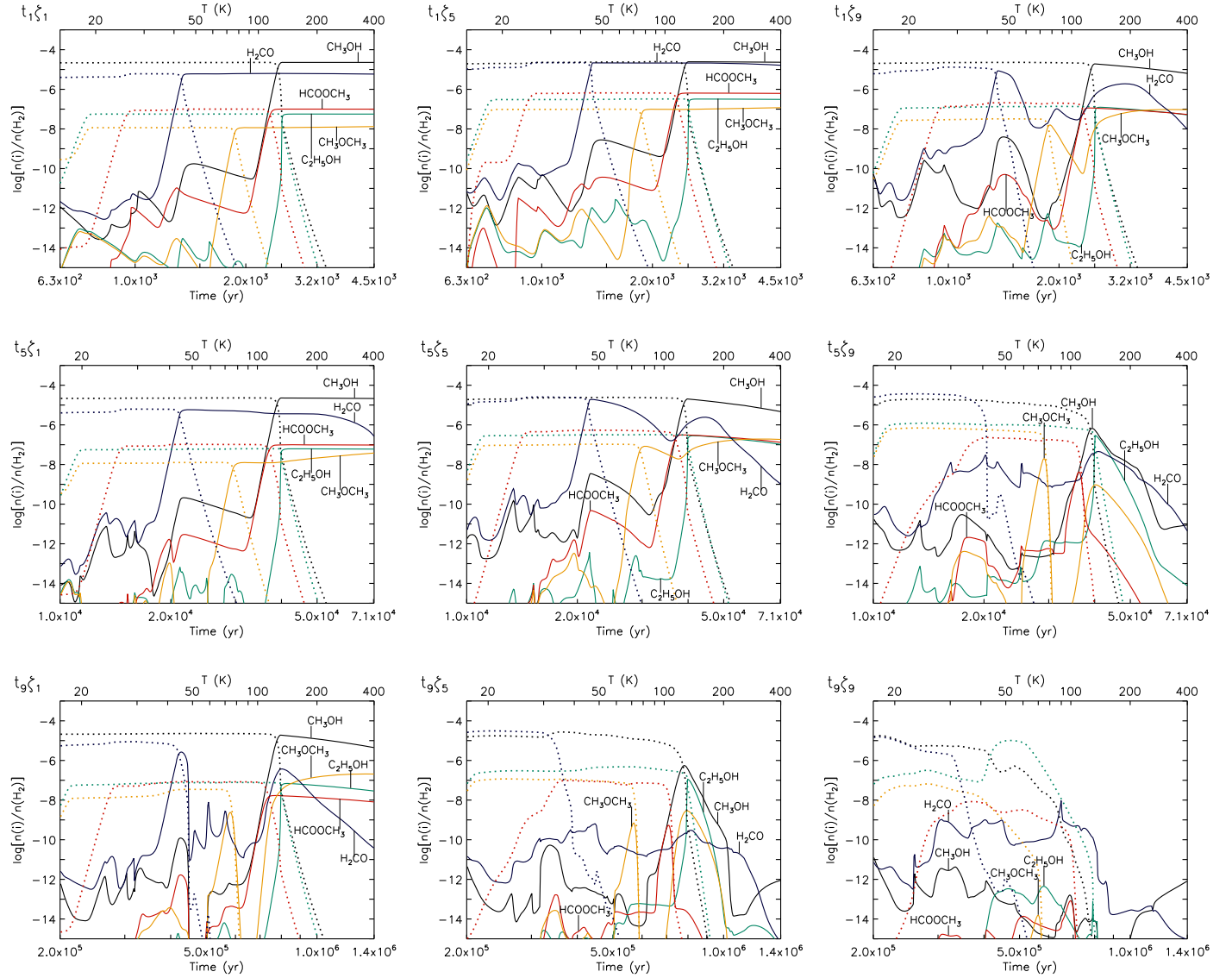


Figure 2. Select time- and temperature-dependent fractional abundance plots (with respect to H_2) for methanol (black), formaldehyde (blue), methyl formate (red), ethanol (green), and dimethyl ether (yellow). Dotted lines represent the sum of grain-surface and ice-mantle abundances, whereas solid lines represent gas-phase abundances. Fractional abundances, time, and temperature (upper axis) are plotted logarithmically.

COMs on the grains, including acetaldehyde, ethanol, dimethyl ether, and methyl formate.

Methanol desorbs in these models at around 110 K, and its gas-phase abundances remain mostly largely unchanged up to 400 K in the $t_{wu} = t_1$ models (Figure 2, panels $t_1\zeta_1$, $t_1\zeta_5$, $t_1\zeta_9$), which provide too little time to permit appreciable changes in abundance. However, for larger t_{wu} and especially large ζ , gas abundances are strongly diminished following thermal desorption of methanol (panels $t_5\zeta_9$, $t_9\zeta_5$, $t_9\zeta_9$). Gas-phase methanol destruction proceeds with the protonation of methanol by $H^3O_{(g)}^+$ to form $CH_3OH_2^+_{(g)}$. The latter recombines to give a variety of products with branching ratios following Geppert et al. (2006). Large ζ results in large abundances of $H^3O_{(g)}^+$, as it is formed indirectly following cosmic-ray ionization of $H_{2(g)}$.

The largest grain and gas peak fractional abundances of methanol with respect to total hydrogen are both around 1×10^{-5} and occur for small to medium ζ (Figure 2, $t_1\zeta_1$, $t_1\zeta_5$, $t_5\zeta_1$, $t_5\zeta_5$, $t_9\zeta_9$). Large abundances result from low influence of the grain-surface and gas-phase destruction reactions.

Conversely, the smallest grain and gas peak fractional abundances are around 9×10^{-6} and 6×10^{-11} , respectively, and occur for $t_{wu} = t_9$ and $\zeta = \zeta_9$ (panel $t_9\zeta_9$).

3.1.2. Formaldehyde

Like methanol, formaldehyde forms on grains during the collapse stage by successive hydrogenation of $CO_{(s)}$. Likewise, its grain abundances are static until desorption for most conditions except for $t_{wu} = t_9$ and $\zeta = \zeta_9$ (Figure 2, panel $t_9\zeta_9$). Abundances are diminished at 30 K for those models, due to H abstraction by $OH_{(s)}$ to form $HCO_{(s)}$, which is a barrierless process.

Formaldehyde desorbs at 40 K, and its post-desorption gas abundances remain static up to 400 K for models with $t_{wu} = t_1$ and small to medium ζ (Figure 2, panels $t_1\zeta_1$, $t_1\zeta_5$). For larger t_{wu} and ζ (panels $t_5\zeta_9$, $t_9\zeta_5$, $t_9\zeta_9$), reaction with $H_{(g)}$ and $O_{(g)}$ destroys gas-phase formaldehyde to produce $HCO_{(g)}$; gas-phase abundances of atomic hydrogen and oxygen are larger

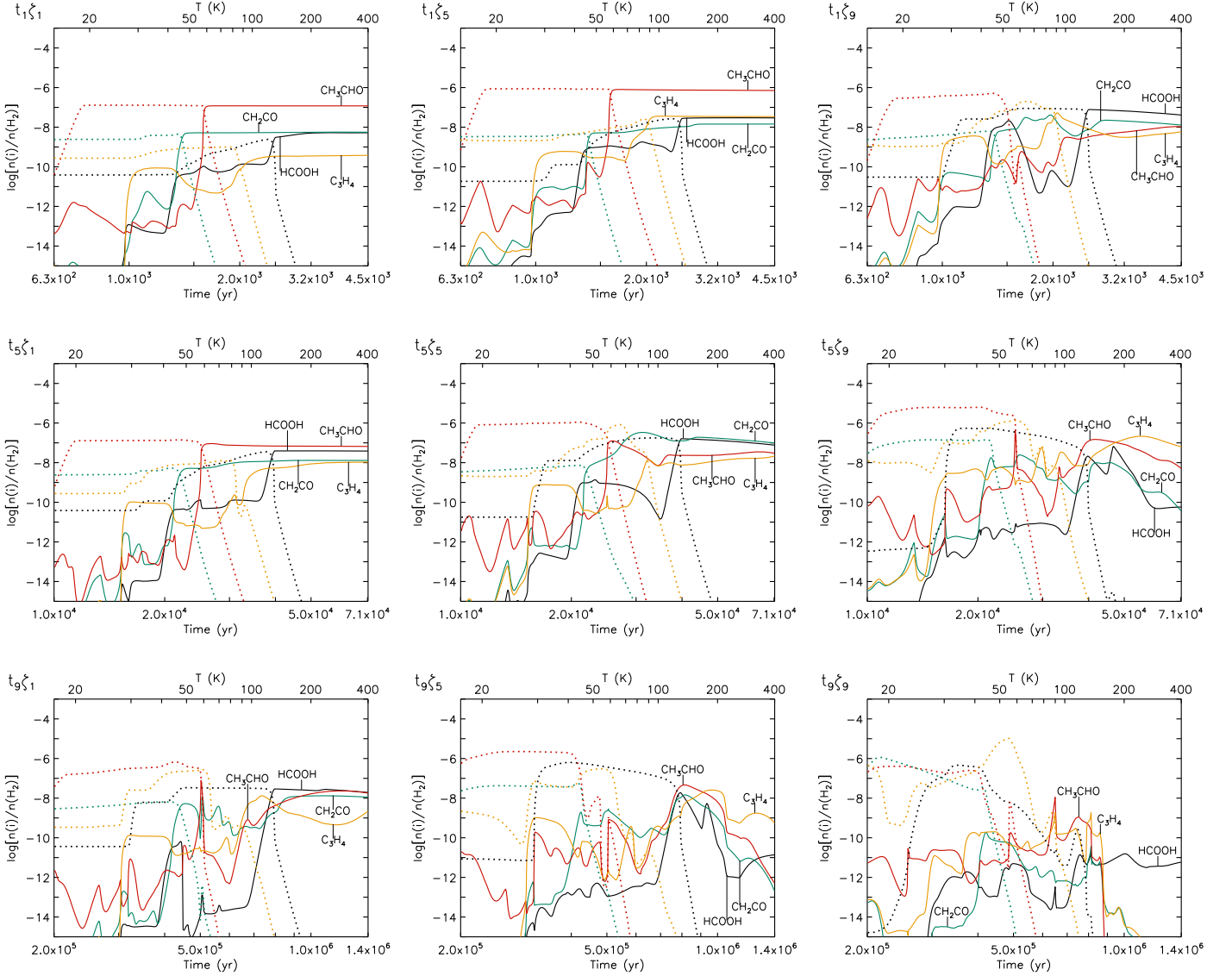
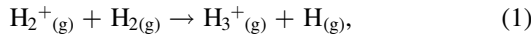
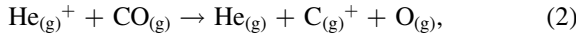


Figure 3. Select time- and temperature-dependent fractional abundance plots (with respect to H_2) for formic acid (black), acetaldehyde (red), ketene (green), and C_3H_4 (yellow). Dotted lines represent the sum of grain-surface and ice-mantle abundances, whereas solid lines represent gas-phase abundances. Fractional abundances, time, and temperature (upper axis) are plotted logarithmically.

for greater ζ values. A surplus of $H_{(g)}$ forms following the reaction

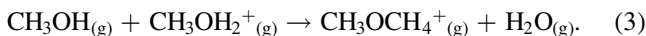


which is more rapid owing to more frequent cosmic-ray ionization of $H_{2(g)}$. $O_{(g)}$ forms via reaction



which is more rapid owing to more frequent cosmic-ray ionization of $He_{(g)}$.

Some models lead to a peak in gas-phase formaldehyde at 110–200 K (Figure 2, panels $t_1\zeta_9$, $t_5\zeta_5$, $t_9\zeta_1$). For these models, gas-phase methanol abundances are large, which permits efficient formation of protonated dimethyl ether, via the reaction



As well as forming a small fraction of dimethyl ether, in the G13 network the recombination of protonated dimethyl

ether with electrons is allowed to produce formaldehyde:



The largest peak formaldehyde abundances on the grains are around 2×10^{-5} and occur for $t_{wu} = t_5$ and $\zeta = \zeta_9$ (Figure 2, panel $t_5\zeta_9$). The largest peak gas-phase abundances are around 1×10^{-5} and occur for $t_{wu} = t_1$ and $\zeta = \zeta_5$ (panel $t_1\zeta_5$). The smallest peak grain abundances are about 2×10^{-6} and occur for $t_{wu} = t_1$ and $\zeta = \zeta_1$ (panel $t_1\zeta_1$). The smallest peak gas-phase abundances are about 3×10^{-10} and occur for $t_{wu} = t_9$ and $\zeta = \zeta_5$ owing to the high influence of gas-phase H-abstraction reactions.

3.1.3. Formic Acid

Two formation schemes generate formic acid in the warm-up phase (Figure 3). At ~ 30 K it forms on grains according to the reaction



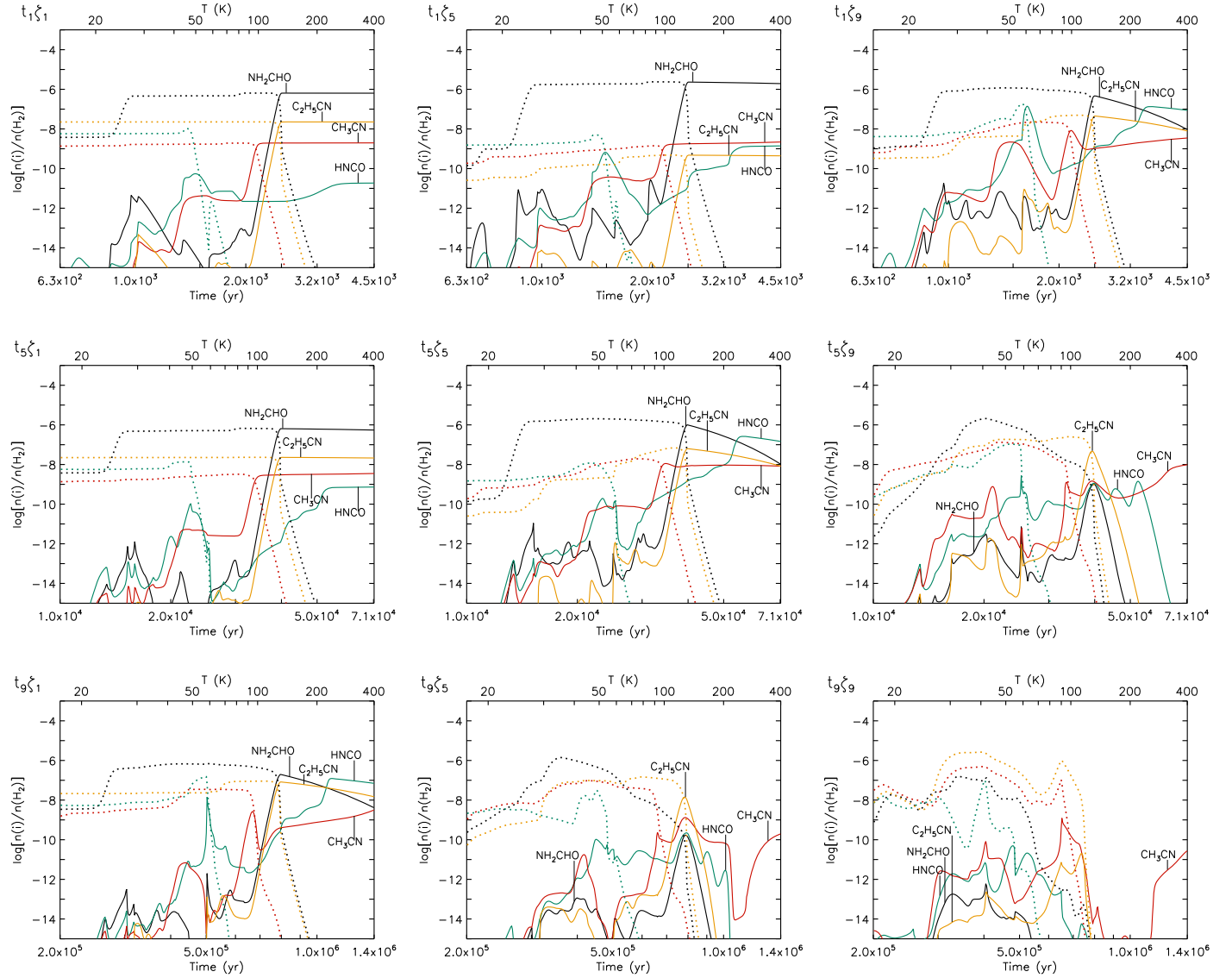
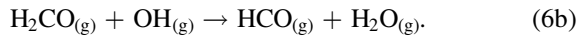


Figure 4. Select time- and temperature-dependent fractional abundance plots (with respect to H_2) for formamide (black), methyl cyanide (red), isocyanic acid (green), and ethyl cyanide (yellow). Dotted lines represent the sum of grain-surface and ice-mantle abundances, whereas solid lines represent gas-phase abundances. Fractional abundances, time, and temperature (upper axis) are plotted logarithmically.

which was suggested by Allen & Robinson (1977). At around 40 K, the thermal desorption of grain-surface formaldehyde promotes rapid reaction with the radical OH through the reactions



Reaction (6a) produces a spike in gas-phase formic acid abundance that is dissipated both by ion-molecule destruction mechanisms and by accretion of $HCOOH$ back onto the grains; the high binding energy of formic acid then allows it to remain on the grains to high temperatures. The alternative branch, Reaction (6b), produces water and the HCO radical. The chemical network used in the model adopts a branching ratio for Reactions (6a) to (6b) of 1:50 (Yetter et al. 1989; DeMore et al. 1997), yet more recent studies suggest that the efficiency

of Reaction (6a) may still be too high (Alvarez-Idaboy et al. 2001; Ocaña et al. 2017; Zanchet et al. 2018; see Section 4).

The production of formic acid through the above reactions increases with greater ζ values. The total rate of Reaction (5) increases with ζ as elevated CRPD of formaldehyde and water ices produces more $HCO_{(s)}$ and $OH_{(s)}$ respectively. Production through Reaction (6a) increases with ζ as the higher rate of CR-induced dissociation of water produces more $OH_{(s)}$, some of which which desorbs into the gas. Combined, these reactions contribute to larger abundances of solid-phase $HCOOH$ at 30–40 K for $\zeta = \zeta_9$ (panels $t_1\zeta_9$, $t_5\zeta_9$, $t_9\zeta_9$). However, at temperatures above 50 K, H abstraction by $OH_{(s)}$, which is the dominant destruction pathway on grains, destroys much formic acid for large t_{wu} and ζ (panels $t_5\zeta_9$, $t_9\zeta_5$, $t_9\zeta_9$). Consequently, abundances are diminished at high temperatures, and the large grain abundances at 40 K do not translate to large gas abundances later in the warm-up.

Formic acid thermally desorbs at around 120 K, and its gas abundances are mostly static for small t_{wu} and for small ζ until

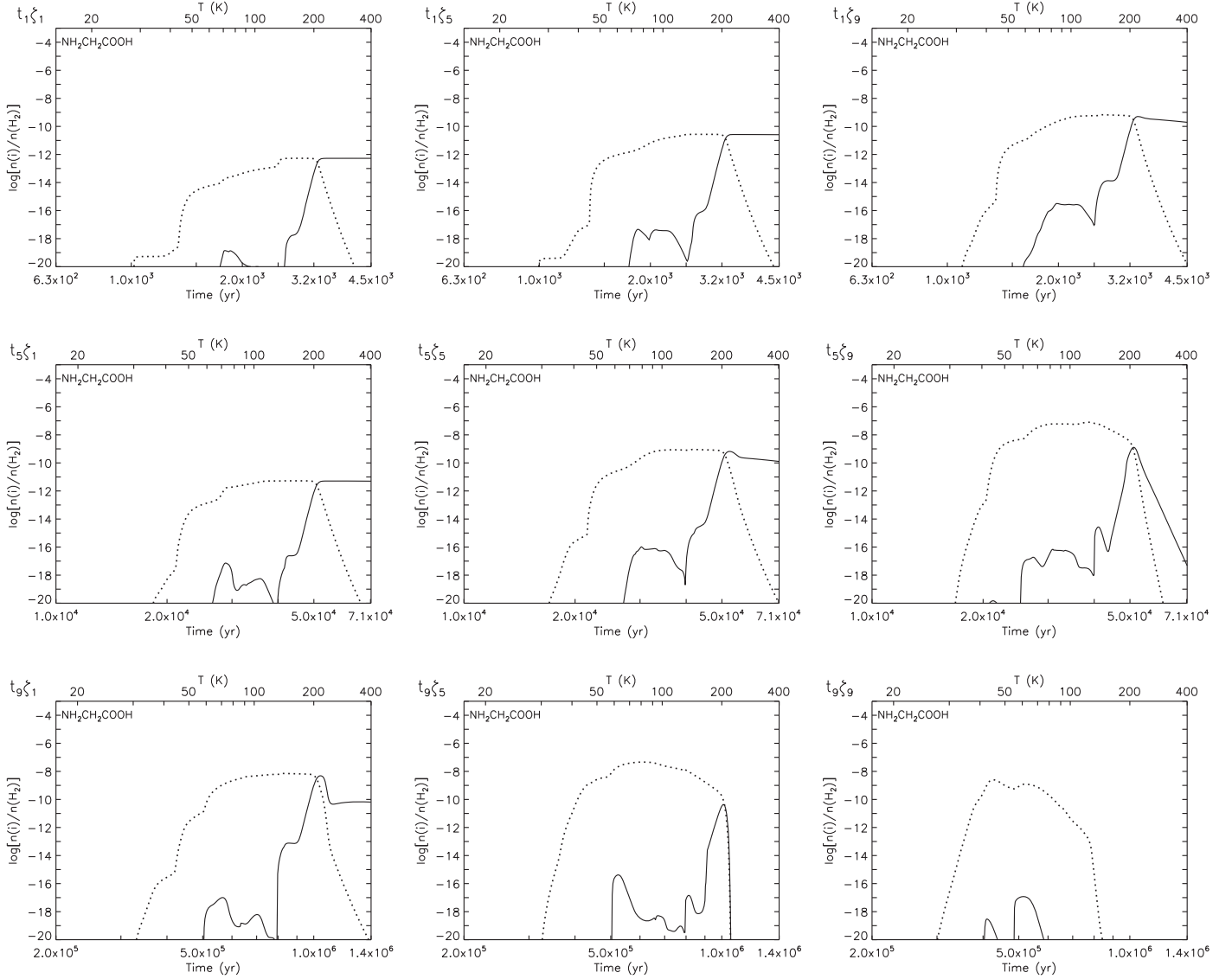


Figure 5. Select time- and temperature-dependent fractional abundance plots (with respect to H_2) for glycine. The dotted line represents the sum of grain-surface and ice-mantle abundances, whereas the solid line represents the gas-phase abundance. The fractional abundance, time, and temperature (upper axis) are plotted logarithmically.

400 K (Figure 3, panels $t_1\zeta_1$, $t_1\zeta_5$, $t_1\zeta_9$, $t_5\zeta_1$, $t_9\zeta_1$). For other conditions, especially those of large t_{wu} and ζ (panel $t_9\zeta_9$), gas-phase formic acid is strongly destroyed by protonation with $H^3O_{(g)}^+$, which leads to diminished abundances.

The largest peak solid-phase abundances are about 3×10^{-7} and occur for $t_{wu} = t_9$ and $\zeta = \zeta_5$ (Figure 3, panel $t_9\zeta_5$). For these conditions, Reactions (5) and 6(a) are efficient and have much time to produce formic acid on grains. Largest peak gas abundances are about 8×10^{-8} and occur for $t_{wu} = t_5$ and $\zeta = \zeta_5$ (panel $t_5\zeta_5$). Smallest peak grain abundances are about 1×10^{-9} and occur for $t_{wu} = t_1$ and $\zeta = \zeta_1$ (panel $t_1\zeta_1$) owing to the low influence of Reactions (5) and 6(a) and a brief period of formation. Smallest peak gas abundances are about 1×10^{-11} and occur for $t_{wu} = t_9$ and $\zeta = \zeta_9$ (panel $t_9\zeta_9$) owing to the high influence of protonation with $H^3O_{(g)}^+$.

3.1.4. Acetaldehyde

Acetaldehyde (CH_3CHO) production on grains during the warm-up phase starts to increase significantly beyond

temperatures of around 12 K, peaking at ~ 20 K (see Figure 3), through the reaction



as well as through hydrogenation of $CH_2CHO_{(s)}$. The production rates for these reactions increase with ζ owing to greater production of the reactants, producing larger solid-phase acetaldehyde abundances with increasing ζ for all but the largest t_{wu} (panels $t_1\zeta_9$, $t_5\zeta_9$). The solid-phase abundances are mostly static from 20 K until desorption for all but large t_{wu} and medium to large ζ (panels $t_9\zeta_5$, $t_9\zeta_9$). For these conditions, CRPD of acetaldehyde and H abstraction by $OH_{(s)}$ and $NH_{2(s)}$ to form radicals $CH_3CO_{(s)}$, $CH_2CHO_{(s)}$, $CH_3_{(s)}$, and $HCO_{(s)}$, are efficient and diminish solid-phase acetaldehyde abundances at temperatures around 40 K.

Acetaldehyde desorbs at about 55 K, and its abundances remain static for small to medium t_{wu} and ζ until 400 K (Figure 3, panels $t_1\zeta_1$, $t_1\zeta_5$, $t_5\zeta_1$). For medium to large t_{wu} and small to medium ζ (panels $t_5\zeta_5$, $t_5\zeta_9$, $t_9\zeta_1$, $t_9\zeta_5$), gas abundances

increase at ~ 100 K owing to the reaction



This reaction is efficient for larger t_{wu} owing to the extended period in which to form $\text{C}_2\text{H}_{5(\text{g})}$. This radical is produced on the grains, from the abstraction of hydrogen from ethane (C_2H_6) by the OH radical, or by the addition of a hydrogen atom to C_2H_4 . The resultant $\text{C}_2\text{H}_{5(\text{s})}$ then desorbs into the gas phase. For all other conditions, $\text{HCO}_{(\text{g})}^+$ and $\text{H}^3\text{O}_{(\text{g})}^+$ protonate and destroy gas-phase acetaldehyde appreciably throughout the warm-up. This effect is most severe for $t_{\text{wu}} = t_9$ and $\zeta = \zeta_9$ (panel $t_9\zeta_9$).

The largest peak solid-phase abundances are $\sim 3 \times 10^{-6}$ and occur for $t_{\text{wu}} = t_5$ and $\zeta = \zeta_9$ (Figure 3, panel $t_5\zeta_9$). For these conditions, Reaction (7) and hydrogenation of $\text{CH}_2\text{CHO}_{(\text{s})}$ are very efficient, whereas CRPD and H abstraction reactions, while also efficient, do not have enough time to greatly diminish abundances. The largest peak gas-phase abundances are $\sim 4 \times 10^{-7}$ and occur for $t_{\text{wu}} = t_1$ and $\zeta = \zeta_5$ (panel $t_1\zeta_5$). The smallest peak solid-phase abundances are $\sim 6 \times 10^{-8}$ and occur for $t_{\text{wu}} = t_1$ and $\zeta = \zeta_1$ (panel $t_1\zeta_1$). The time period available to form acetaldehyde is very brief under these conditions. The smallest peak gas-phase abundances are $\sim 5 \times 10^{-9}$ and occur for $t_{\text{wu}} = t_9$ and $\zeta = \zeta_9$ (panel $t_9\zeta_9$) owing to the high influence of protonation reactions.

3.1.5. Ketene

Much ketene (CH_2CO) forms on grains during the collapse phase by successive hydrogenation of $\text{C}_2\text{O}_{(\text{s})}$ that originates in the gas phase, although some ketene also forms in the warm-up, via CRPD of $\text{CH}_2\text{CHO}_{(\text{s})}$ (Figure 3). $\text{CH}_2\text{CHO}_{(\text{s})}$ forms at low temperatures via the addition of $\text{CH}_{2(\text{s})}$ and $\text{HCO}_{(\text{s})}$ radicals, which are formed mostly from CRPD of methane and formaldehyde, respectively. This mechanism elevates solid-phase ketene abundances slightly throughout the warm-up phase up until desorption, for most model setups. However, for $t_{\text{wu}} = t_9$ and $\zeta = \zeta_9$ (panel $t_9\zeta_9$), CRPD of ketene to $\text{CH}_{2(\text{s})}$ and $\text{CO}_{(\text{s})}$ diminishes abundances until desorption. This is the strongest grain-surface destruction mechanism, and it is more effective than formation reactions for these conditions, producing a net loss.

Ketene desorbs at ~ 45 K, and its gas-phase abundances remain mostly static for small to medium t_{wu} and ζ until 400 K (Figure 3, panels $t_1\zeta_1$, $t_1\zeta_5$, $t_5\zeta_1$). In some models, ketene may be formed in appreciable quantities as a product of the dissociative electronic recombination of protonated dimethyl ether (at around 60–70 K), which elevates abundances particularly for panels $t_1\zeta_9$ and $t_5\zeta_5$. Ketene may also form late in the warm-up, starting at ~ 130 K, as the product of electronic recombination of protonated acetic acid ($\text{CH}_3\text{COOH}_2^+$), which elevates abundances somewhat for models $t_5\zeta_9$, $t_9\zeta_1$, and $t_9\zeta_5$. Gas-phase abundances are otherwise diminished at medium to high t_{wu} and ζ (panels $t_5\zeta_9$, $t_9\zeta_5$, $t_9\zeta_9$) owing to protonation by $\text{HCO}_{(\text{g})}^+$ and $\text{H}^3\text{O}_{(\text{g})}^+$. However, the product branching ratios for neither of the above-mentioned dissociative recombination processes are well constrained, so the gas-phase formation of ketene during the warm-up phase should be treated with some caution.

The largest peak solid-phase abundances are $\sim 6 \times 10^{-7}$ and occur for $t_{\text{wu}} = t_9$ and $\zeta = \zeta_9$ (Figure 3, panel $t_9\zeta_9$). The largest gas-phase abundances are $\sim 2 \times 10^{-7}$ and occur for $t_{\text{wu}} = t_5$

and $\zeta = \zeta_5$ (panel $t_5\zeta_5$). These intermediate models mark the conditions at which formation reactions are most efficient compared to destruction reactions. The smallest peak solid-phase abundances are $\sim 2 \times 10^{-9}$ and occur for $t_{\text{wu}} = t_1$ and $\zeta = \zeta_1$ (panel $t_1\zeta_1$). Here, formation reactions have low influence and the period of formation is brief. The smallest gas-phase abundances are $\sim 9 \times 10^{-11}$ and occur for $t_{\text{wu}} = t_9$ and $\zeta = \zeta_9$ owing to the high influence of destruction reactions.

3.1.6. Methyl Acetylene

B07 observe methyl acetylene (CH_3CCH) in their survey; however, the chemical network used here does not explicitly distinguish it from the other stable linear structural isomer of formula C_3H_4 , propadiene (CH_2CCH_2). In the description of the models, we will therefore refer simply to C_3H_4 .

C_3H_4 is first formed appreciably in the gas phase at around 30 K and then accreted onto grains (Figure 3). At this temperature, methane reacts with $\text{C}^+_{(\text{g})}$ and $\text{H}_3^+_{(\text{g})}$, as well as with the products of these reactions, to form a variety of neutral and ionic hydrocarbons. Among them are $\text{C}_3\text{H}_5^+_{(\text{g})}$ and $\text{C}_4\text{H}_5^+_{(\text{g})}$, which recombine with electrons to form $\text{C}_3\text{H}_{4(\text{g})}$. Some C_3H_4 also forms on grains at low temperatures via hydrogenation of related hydrocarbons. These formation reactions gradually build up the grain-surface abundances, until C_3H_4 eventually desorbs. The gas-phase reactions become more effective in producing C_3H_4 under conditions of greater ζ , since ionic abundances are larger, resulting in greater abundances on the grains for all t_{wu} (models $t_1\zeta_9$, $t_5\zeta_9$, $t_9\zeta_9$).

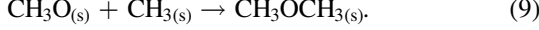
Following desorption of C_3H_4 at 80 K, there remain a few mechanisms by which it continues to be formed in the gas phase; the strongest of these include the electronic recombination of protonated propylene and protonated propanal. The production of C_3H_4 through these reactions increases with ζ , owing to the greater protonation rates of the precursor molecules by abundant molecular ions. As a result, these reactions elevate gas-phase C_3H_4 abundances at temperatures greater than 100 K for some models with medium to large ζ (Figure 3, panels $t_5\zeta_9$, $t_9\zeta_5$). As with ketene, the uncertainty in the dissociation products of large molecular ions means that the higher-temperature gas-phase production routes should be viewed with some caution. Despite the influence of these reactions, gas-phase abundances of C_3H_4 are generally diminished for large t_{wu} and ζ (panel $t_9\zeta_9$) owing to protonation by $\text{H}^3\text{O}_{(\text{g})}^+$.

The largest peak grain abundances are $\sim 5 \times 10^{-6}$ and occur for models with $t_{\text{wu}} = t_9$ and $\zeta = \zeta_9$ (Figure 3, panel $t_9\zeta_9$) since the low-temperature formation reactions are efficient and have a long time to form C_3H_4 . The largest peak gas-phase abundances are $\sim 1 \times 10^{-7}$ and occur for $t_{\text{wu}} = t_5$ and $\zeta = \zeta_9$ (panel $t_5\zeta_9$). In this case, all formation reactions are much more effective than the gas-phase destruction reaction. The smallest peak grain and gas-phase abundances are $\sim 5 \times 10^{-10}$ and $\sim 2 \times 10^{-10}$, respectively, and occur for $t_{\text{wu}} = t_1$ and $\zeta = \zeta_1$ (panel $t_1\zeta_1$), under which conditions the formation reactions are inefficient and the formation time is brief.

3.1.7. Dimethyl Ether

Dimethyl ether (CH_3OCH_3) begins to form on grains early in the warm-up stage, peaking at around 20 K (see Figure 2),

through the reaction



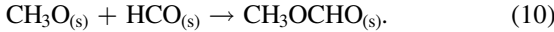
This reaction is more effective at higher ζ values, as the reactants are formed from CRPD of methanol. Consequently, grain-surface abundances increase with ζ , particularly for small and medium t_{wu} (panels $t_1\zeta_1$, $t_1\zeta_5$, $t_1\zeta_9$, $t_5\zeta_1$, $t_5\zeta_5$, $t_5\zeta_9$). After formation, grain abundances remain static for most conditions until desorption. However, for $t_{\text{wu}} = t_9$ and $\zeta = \zeta_9$ (panel $t_9\zeta_9$), CRPD diminishes abundances at temperatures greater than 30 K. Although this is not the only destruction reaction on grains, it is the strongest.

Dimethyl ether desorbs at 70 K, and its gas abundances remain static for small t_{wu} and small to medium ζ until 400 K (Figure 2, panels $t_1\zeta_1$, $t_1\zeta_5$). Dimethyl ether can also form in the gas phase from methanol, via Reaction (3) followed by dissociative electronic recombination of $\text{CH}_3\text{OCH}_4^+_{(\text{g})}$. This scheme leads to a gas-phase peak at ~ 110 K for certain conditions (models $t_1\zeta_9$, $t_5\zeta_5$, $t_5\zeta_9$, $t_9\zeta_1$, $t_9\zeta_5$). Although the efficiency of this dissociative recombination in producing dimethyl ether is likely very low (Hamberg et al. 2010), a large abundance of gas-phase methanol, derived from the grains, can make it very effective. Dimethyl ether is destroyed in the gas phase via protonation by $\text{HCO}_{(\text{g})}^+$ and $\text{H}^3\text{O}_{(\text{g})}^+$ (again, followed by dissociative recombination), which diminishes abundances particularly for large t_{wu} and ζ (panel $t_9\zeta_9$).

The largest peak grain-surface abundances of dimethyl ether are $\sim 4 \times 10^{-7}$ and occur for $t_{\text{wu}} = t_5$ and $\zeta = \zeta_9$ (Figure 2, panel $t_5\zeta_9$) owing to the high influence of Reaction (9). Largest peak gas abundances are about 1×10^{-7} and occur for $t_{\text{wu}} = t_9$ and $\zeta = \zeta_1$ (panel $t_9\zeta_1$) owing to the high influence of Reaction (3). The smallest peak grain-surface abundances are $\sim 6 \times 10^{-9}$ and occur for $t_{\text{wu}} = t_9$ and $\zeta = \zeta_1$. The smallest peak gas-phase abundances are $\sim 8 \times 10^{-15}$ and occur for model $t_9\zeta_9$ owing to rapid grain-surface and gas-phase destruction reactions.

3.1.8. Methyl Formate

Methyl formate forms on grains during the warm-up from 15 to 25 K (Figure 2) via the reaction



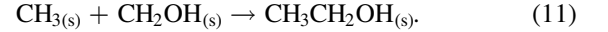
Grain abundances remain static thereafter until desorption for most models. However, for large t_{wu} and ζ (panel $t_9\zeta_9$) abundances are diminished at temperatures greater than 40 K, primarily due to H-abstraction reactions. Methyl formate is first destroyed at about 40 K owing to H abstraction by $\text{OH}_{(\text{s})}$ to form $\text{CH}_3\text{OCO}_{(\text{s})}$ and water. Some of the $\text{CH}_3\text{OCO}_{(\text{s})}$ produced rehydrogenates to methyl formate, though the rate of methyl formate destruction typically exceeds the rate of reformation by a factor of several. Beginning at 60 K, H abstraction by $\text{NH}_{2(\text{s})}$ becomes the strongest destruction pathway, again with some rehydrogenation to methyl formate.

Methyl formate desorbs at about 100–110 K, and its gas abundances remain mostly static for small t_{wu} and ζ (Figure 2, panels $t_1\zeta_1$, $t_1\zeta_5$, $t_1\zeta_9$, $t_5\zeta_1$, $t_9\zeta_1$) until 400 K. However, for all other models, gas-phase methyl formate is destroyed appreciably by protonation with $\text{HCO}_{(\text{g})}^+$ and $\text{H}^3\text{O}_{(\text{g})}^+$. The rate of destruction is especially high for large ζ and diminishes abundances most dramatically for large t_{wu} (panel $t_9\zeta_9$).

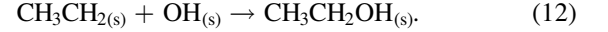
The largest peak solid-phase abundances are $\sim 4 \times 10^{-7}$ and occur for $t_{\text{wu}} = t_1$ and $\zeta = \zeta_5$ (Figure 2, panel $t_1\zeta_5$) owing to the high influence of Reaction (10) and the low influence of H abstraction reactions. The largest peak gas-phase abundances are $\sim 2 \times 10^{-7}$ and occur for $t_{\text{wu}} = t_5$ and $\zeta = \zeta_5$ (panel $t_5\zeta_5$) also owing to the high influence of Reaction (10) and the low influence of H abstraction reactions. The smallest peak grain-surface and gas-phase abundances are $\sim 3 \times 10^{-7}$ and 4×10^{-14} , respectively, and occur for $t_{\text{wu}} = t_9$ and $\zeta = \zeta_9$ (panel $t_9\zeta_9$), since both the H-abstraction reactions on grains and the protonation reactions in the gas phase are most efficient.

3.1.9. Ethanol

B07 suggest that ethanol ($\text{C}_2\text{H}_5\text{OH}$) may be formed on grains by hydrogenation of ketene and acetaldehyde, though we lack these pathways in our network. In the present models (see Figure 2), ethanol forms on grains during the warm-up between 13 and 20 K, via the reaction



At 40 K, ethanol is also formed on grains via



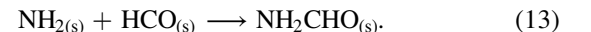
The rates of these reactions increase with ζ and produce larger grain abundances for all t_{wu} (panels $t_1\zeta_9$, $t_5\zeta_9$, $t_9\zeta_9$). Reaction (12) is particularly efficient for large timescales, as there is adequate time to form $\text{CH}_3\text{CH}_2_{(\text{s})}$, which mostly originates from the hydrogenation of $\text{C}_2\text{H}_{(\text{s})}$. Consequently, a large solid-phase abundance peak occurs from 40 to 60 K for $t_{\text{wu}} = t_9$ and $\zeta = \zeta_9$ (panel $t_9\zeta_9$). Solid-phase abundances are static until desorption for most models; however, for large t_{wu} and ζ (panel $t_9\zeta_9$), ethanol abundances on the grains are diminished at temperatures greater than 60 K, primarily due to H abstraction by $\text{OH}_{(\text{s})}$ to form $\text{C}_2\text{H}_5\text{O}_{(\text{s})}$ and water ice.

Ethanol desorbs at 110 K, and its gas-phase abundances remain mostly static for small t_{wu} and ζ (Figure 2, panels $t_1\zeta_1$, $t_1\zeta_5$, $t_1\zeta_9$, $t_5\zeta_1$, $t_9\zeta_1$) until 400 K. For other conditions, it is destroyed efficiently via protonation by $\text{H}^3\text{O}_{(\text{g})}^+$, which diminishes gas-phase ethanol abundances. This effect is pronounced for large t_{wu} and ζ (panel $t_9\zeta_9$).

The largest peak solid-phase abundances are $\sim 5 \times 10^{-6}$ and occur for $t_{\text{wu}} = t_9$ and $\zeta = \zeta_9$ (Figure 2, panel $t_9\zeta_9$) owing to the high influence of Reaction (12) and especially Reaction (13). The largest peak gas-phase abundances are $\sim 2 \times 10^{-7}$ and occur for $t_{\text{wu}} = t_1$ and $\zeta = \zeta_5$ (panel $t_1\zeta_5$). For these conditions, the influence of protonation by $\text{H}^3\text{O}_{(\text{g})}^+$ is low, which allows for a large gas-phase peak. The smallest peak grain-surface abundances are $\sim 3 \times 10^{-8}$ and occur for $t_{\text{wu}} = t_1$ and $\zeta = \zeta_1$ (panel $t_1\zeta_1$). The smallest peak gas-phase abundances are $\sim 2 \times 10^{-13}$ and occur for $t_{\text{wu}} = t_9$ and $\zeta = \zeta_9$, due to the high influence of protonation by $\text{H}^3\text{O}_{(\text{g})}^+$.

3.1.10. Formamide

Formamide (NH_2CHO) forms on the grains at temperatures around 20–30 K (see Figure 4) via the reaction



Grain abundances are static thereafter until desorption, for most models. However, for medium to large t_{wu} and ζ (panels $t_5\zeta_9$,

$t_9\zeta_5$, $t_9\zeta_9$), formamide is destroyed at temperatures greater than 60 K, primarily due to H abstraction by $\text{NH}_{2(s)}$ to form $\text{NH}_2\text{CO}_{(s)}$ and ammonia. Some $\text{NH}_2\text{CO}_{(s)}$ rehydrogenates to formamide, though the reformation rate is up to one order of magnitude smaller than the H abstraction rate. Consequently, solid-phase abundances are diminished for these conditions.

Formamide desorbs at 110 K and remains static in the gas phase for small to medium t_{wu} and ζ (Figure 4, panels $t_1\zeta_1$, $t_1\zeta_5$, $t_5\zeta_1$) until 400 K. It is efficiently destroyed in the gas phase for all other conditions via protonation by $\text{H}^3\text{O}_{(g)}^+$. This reaction diminishes gas-phase abundances, especially for large t_{wu} and ζ (panel $t_9\zeta_9$).

The largest peak solid- and gas-phase abundances are both $\sim 1 \times 10^{-6}$ and occur for $t_{\text{wu}} = t_1$ and $\zeta = \zeta_5$ (Figure 4, panel $t_1\zeta_5$) owing to the low influence of destruction reactions. The smallest peak solid- and gas-phase abundances are $\sim 8 \times 10^{-8}$ and $\sim 3 \times 10^{-13}$, respectively, and occur for $t_{\text{wu}} = t_9$ and $\zeta = \zeta_9$ (panel $t_9\zeta_9$).

It may be noted that the chemical network does not include the reaction between NH_2 and formaldehyde that has been suggested as a possible gas-phase formation mechanism for formamide (Barone et al. 2015). Production of formamide through Reaction (13) in the present model appears more than sufficient to reproduce observational abundances (see later sections). The efficiency of the reaction is also subject to some doubt (Song & Kästner 2016).

3.1.11. Isocyanic Acid

Isocyanic acid (HNCO) forms on grains during the collapse and warm-up phases by the hydrogenation of $\text{OCN}_{(s)}$ (Figure 4). This process becomes more efficient with increasing ζ , due to increased abundances of $\text{OCN}_{(s)}$, which forms in the gas phase through ion-molecule reactions involving $\text{HCN}_{(g)}$. Hydrogenation of OCN elevates solid-phase abundances of isocyanic acid over the temperature range 15–60 K, especially for some large- ζ models (panels $t_1\zeta_9$, $t_5\zeta_9$).

Isocyanic acid desorbs at about 60 K, and its gas-phase abundances tend to increase in the temperature range of 100–400 K for most models (see Figure 4). Several reactions contribute to the increase, most importantly one of the branches for the dissociative electronic recombination of protonated urea, in line with other studies (Garrod et al. 2008; Tideswell et al. 2010). Formation of HNCO through this mechanism becomes more important with increasing ζ , since there are more ions to protonate urea ($\text{NH}_2\text{CONH}_{2(g)}$). As a result, isocyanic acid gas-phase abundances tend to increase with ζ for small t_{wu} , and somewhat for medium t_{wu} (panels $t_1\zeta_1$, $t_1\zeta_5$, $t_1\zeta_9$, $t_5\zeta_1$, $t_5\zeta_5$). Gas-phase production of HNCO also increases with greater t_{wu} (panels $t_1\zeta_1$, $t_5\zeta_1$, $t_9\zeta_1$, $t_5\zeta_1$, $t_5\zeta_5$). However, as t_{wu} and ζ increase, protonation by $\text{HCO}_{(g)}^+$ and $\text{H}^3\text{O}_{(g)}^+$ becomes efficient and diminishes gas abundances (panels $t_5\zeta_9$, $t_9\zeta_5$, $t_9\zeta_9$).

The largest peak solid-phase abundances are $\sim 9 \times 10^{-8}$ and occur for $t_{\text{wu}} = t_1$ and $\zeta = \zeta_9$ (Figure 4, panel $t_1\zeta_9$). The largest peak gas-phase abundances are $\sim 6 \times 10^{-8}$ and occur for $t_{\text{wu}} = t_9$ and $\zeta = \zeta_1$ (panel $t_9\zeta_1$). The smallest peak grain abundances are $\sim 3 \times 10^{-9}$ and occur for $t_{\text{wu}} = t_1$ and $\zeta = \zeta_5$ (panel $t_1\zeta_9$). The smallest peak gas-phase abundances are about 3×10^{-11} and occur for $t_{\text{wu}} = t_9$ and $\zeta = \zeta_9$ (panel $t_9\zeta_9$) owing to the high influence of protonation reactions.

3.1.12. Methyl Cyanide

Methyl cyanide (CH_3CN) forms on grains during the collapse and warm-up by hydrogenation of $\text{CH}_2\text{CN}_{(s)}$ and less hydrogenated forms of $\text{C}_2\text{N}_{(s)}$, as well as through the radical-radical addition reaction



as seen in Figure 4. These reactions are more effective for greater values of ζ , due to larger abundances of reactants, producing increased solid-phase CH_3CN abundances that are greatest for the largest ζ models (panels $t_1\zeta_9$, $t_5\zeta_9$, $t_9\zeta_9$). Conversely, for small ζ models, grain abundances are mostly static until desorption (models $t_1\zeta_1$, $t_5\zeta_1$, $t_9\zeta_1$).

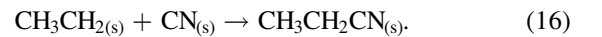
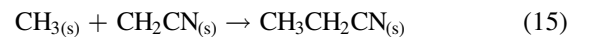
Once methyl cyanide desorbs at about 85 K, its gas abundances remain static for models with small to medium t_{wu} and ζ (Figure 4, panels $t_1\zeta_1$, $t_1\zeta_5$, $t_5\zeta_1$, $t_5\zeta_5$) until 400 K. For models with greater t_{wu} and ζ , methyl cyanide can be formed more efficiently in the gas phase at temperatures greater than ~ 100 K through the radiative association reaction between $\text{CH}_3^+_{(g)}$ and $\text{HCN}_{(g)}$ (Charnley et al. 1992), followed by dissociative electronic recombination of the resultant protonated methyl cyanide. Gas-phase abundances of methyl cyanide tend to increase toward the end of the warm-up as a result ($t_1\zeta_9$, $t_5\zeta_9$, $t_9\zeta_1$, $t_9\zeta_5$, $t_9\zeta_9$). Despite this reaction, gas-phase abundances are diminished overall for large t_{wu} and ζ (panels $t_9\zeta_5$, $t_9\zeta_9$) owing to protonation by $\text{HCO}_{(g)}^+$ and $\text{H}^3\text{O}_{(g)}^+$.

The largest peak solid-phase abundances are $\sim 1 \times 10^{-7}$ and occur for $t_{\text{wu}} = t_9$ and $\zeta = \zeta_9$ (Figure 4, panel $t_9\zeta_9$). Largest peak gas abundances are $\sim 6 \times 10^{-9}$ and occur for $t_{\text{wu}} = t_5$ and $\zeta = \zeta_5$ (panel $t_5\zeta_5$). The smallest peak solid-phase abundances are $\sim 9 \times 10^{-10}$ and occur for $t_{\text{wu}} = t_1$ and $\zeta = \zeta_1$ (panel $t_1\zeta_1$) owing to the inefficiency of formation reactions and the brief period of formation. The smallest peak gas-phase abundances are $\sim 3 \times 10^{-10}$ and occur for $t_{\text{wu}} = t_9$ and $\zeta = \zeta_9$ owing to the high influence of protonation reactions.

3.1.13. Ethyl Cyanide

Ethyl cyanide ($\text{C}_2\text{H}_5\text{CN}$) forms on grains during the collapse stage, via successive hydrogenation of $\text{C}_3\text{N}_{(s)}$ (Figure 4). Destruction of solid-phase ethyl cyanide via CRPD, to form radicals $\text{CH}_3\text{CH}_2(s)$, $\text{CH}_3(s)$, $\text{CN}_{(s)}$, $\text{CH}_2\text{CN}_{(s)}$, $\text{CH}_3\text{CHCN}_{(s)}$, and $\text{CH}_2\text{CH}_2\text{CN}_{(s)}$, also gains in importance for models with greater ζ values. As a result, solid-phase abundances tend to be diminished for large ζ models compared to small ζ models at the beginning of the warm-up phase (panels $t_1\zeta_1$, $t_1\zeta_9$).

Solid-phase ethyl cyanide abundances remain static throughout the warm-up until desorption for small ζ (panels $t_1\zeta_1$, $t_5\zeta_1$, $t_9\zeta_1$). It can also be formed efficiently on grains during the warm-up phase for models with greater ζ values, via the reactions



These reactions are more effective with greater ζ , due to larger abundances of the reactants, which are formed primarily from CRPD of methanol, methane, and $\text{HCN}_{(s)}$. Accordingly, ethyl cyanide abundances gradually increase for medium to large ζ (models $t_1\zeta_9$, $t_5\zeta_5$, $t_5\zeta_9$, $t_9\zeta_5$, $t_9\zeta_9$).

Ethyl cyanide desorbs from the grains at ~ 110 K, and its gas-phase abundances remain mostly static for small t_{wu} (Figure 4, panels $t_1\zeta_1$, $t_1\zeta_5$, $t_1\zeta_9$) and small ζ (panels $t_5\zeta_1$, $t_9\zeta_1$) until 400 K. For all other conditions, it is destroyed efficiently via protonation by $\text{H}^3\text{O}_{(\text{g})}^+$, leading to diminished gas-phase abundances, especially for large t_{wu} and ζ (panel $t_9\zeta_9$).

The largest peak solid-phase abundances are $\sim 1 \times 10^{-6}$ and occur for $t_{\text{wu}} = t_9$ and $\zeta = \zeta_9$ (Figure 4, panel $t_9\zeta_9$) owing to the high influence of Reactions (15) and (16). The largest peak gas-phase abundances are $\sim 4 \times 10^{-8}$ and occur for $t_{\text{wu}} = t_9$ and $\zeta = \zeta_1$ (panel $t_9\zeta_1$) owing to the low influence of the protonation reaction. The smallest peak solid-phase abundances are about 1×10^{-8} and occur for $t_{\text{wu}} = t_1$ and $\zeta = \zeta_1$. The production rates of the reactants that form ethyl cyanide via Reactions (15) and (16) are small in this case, and the formation period is brief. The smallest peak gas-phase abundances are $\sim 1 \times 10^{-11}$ and achieved in the model with $t_{\text{wu}} = t_9$ and $\zeta = \zeta_9$ owing to the high influence of the protonation reaction.

3.1.14. Glycine

Glycine ($\text{NH}_2\text{CH}_2\text{COOH}$), as yet undetected in an interstellar source, in these models forms on grains in the warm-up stage, via the reactions



as well as through hydrogenation of $\text{NHCH}_2\text{COOH}_{(\text{s})}$ (Figure 5). The $\text{NH}_2\text{CH}_2\text{CO}_{(\text{s})}$ radical (Reaction (17)) is formed primarily by H abstraction from glycinal ($\text{NH}_2\text{CH}_2\text{CHO}$). Glycinal itself is mostly formed by the reaction of $\text{CH}_{2(\text{s})}$ and $\text{NH}_{2(\text{s})}$, whose product, $\text{CH}_2\text{NH}_{2(\text{s})}$, reacts with $\text{HCO}_{(\text{s})}$. The $\text{CH}_2\text{COOH}_{(\text{s})}$ radical of Reaction (18) mostly forms from CRPD of acetic acid (CH_3COOH) and through the reaction of $\text{CH}_{2(\text{s})}$ and $\text{HOCO}_{(\text{s})}$. The $\text{NHCH}_2\text{COOH}_{(\text{s})}$ radical forms mostly through the addition reaction of $\text{NH}_{(\text{s})}$ with $\text{CH}_2\text{COOH}_{(\text{s})}$, with $\text{NH}_{(\text{s})}$ produced by CRPD of solid-phase ammonia.

The formation reactions on grains elevate solid-phase glycine abundances appreciably at ~ 30 K (Figure 5). These reactions are more effective for models with greater ζ , as the reactants involved form from CRPD of primary ice constituents. Accordingly, grain abundances grow larger for large ζ compared to small ζ for most t_{wu} (models $t_1\zeta_1$, $t_1\zeta_9$, $t_5\zeta_9$). At large t_{wu} and ζ (panel $t_9\zeta_9$), however, solid-phase abundances are diminished by CRPD to form $\text{NH}_{2(\text{s})}$ and $\text{CH}_2\text{COOH}_{(\text{s})}$, and H abstraction by $\text{OH}_{(\text{s})}$ and $\text{NH}_{2(\text{s})}$ beginning at 40 and 60 K, respectively. In the $t_9\zeta_9$ model, glycine is completely destroyed on the grain surfaces prior to desorption.

Glycine desorbs at ~ 200 K, and its gas-phase abundances remain static for small t_{wu} (Figure 5, panels $t_1\zeta_1$, $t_1\zeta_5$, $t_1\zeta_9$) and mostly static for small ζ (panels $t_5\zeta_1$, $t_9\zeta_1$). However, for all other conditions it is efficiently destroyed via protonation by $\text{H}^3\text{O}_{(\text{g})}^+$, which leads to diminished gas-phase abundances, especially for large t_{wu} and ζ (panel $t_9\zeta_9$). A more extensive discussion of the grain and gas-phase glycine chemistry included in this network is given by G13.

The largest peak solid- and gas-phase abundances for glycine are $\sim 4 \times 10^{-8}$ and $\sim 7 \times 10^{-10}$, respectively, and occur for $t_{\text{wu}} = t_5$ and $\zeta = \zeta_9$ (Figure 5, panel $t_5\zeta_9$) owing to rapid

production and the limited influence of grain and gas-phase destruction reactions. The smallest peak solid-phase abundances are $\sim 3 \times 10^{-13}$ and occur for $t_{\text{wu}} = t_1$ and $\zeta = \zeta_1$ (panel $t_1\zeta_1$). The smallest peak gas-phase abundances are about 6×10^{-18} and occur for $t_{\text{wu}} = t_9$ and $\zeta = \zeta_9$ (panel $t_9\zeta_9$). For these conditions, solid-phase glycine is destroyed almost entirely prior to desorption, due to the high influence of CRPD and H-abstraction reactions.

3.2. Column Densities and Excitation Temperatures

In order to obtain abundance information that can be directly compared with observational data, modeled fractional abundance data from the grid are mapped onto the temperature and density profiles obtained for NGC 6334 IRS 1, NGC 7538 IRS 1, W3(H₂O), and W33A by van der Tak et al. (2000). For each model in the grid, all molecular emission lines observed by B07 for the source in question are simulated using the radiative transfer model, including convolution with the appropriate telescope beam size for the line frequency and the instrument with which it was observed by B07. Integrated intensities for the resultant molecular line spectra are plotted in population diagrams to derive a value for N_{tot} and for T_{ex} , for each molecule, for all chemical models and sources. In order to replicate as precisely as possible the population diagram method carried out by B07, the line-integrated intensities plotted in the population diagrams are rescaled according to the size of the telescope beam at the line frequency (see B07 for details). The line emission is also corrected for optical depth effects, where appropriate, following the correction given by Herbst & van Dishoeck (2009). The radiative transfer calculations automatically provide the optical depth for each frequency channel.

As an example, population diagrams for ethanol are shown in Figure 6, for a selection of chemical models applied to source NGC 6334 IRS 1. N_{tot} generally parallels abundance trends; however, since it represents space-integrated number densities, its value gives a more comprehensive representation of a molecule's abundance throughout the source as a whole. T_{ex} is indicative of temperatures at which peak fractional abundances occur and trends somewhat differently than integrated intensities and N_{tot} . The data are seen to be well represented by a single N_{tot} and T_{ex} value.

For most molecules, N_{tot} values increase from small to large ζ for small t_{wu} models and decrease from small to large ζ for large t_{wu} models. For example, N_{tot} of ethanol for source NGC 6334 IRS 1 increases from $8.7 \times 10^{10} \text{ cm}^{-2}$ to $2.8 \times 10^{15} \text{ cm}^{-2}$ from large to small ζ for $t_{\text{wu}} = t_9$ (Figure 6, panels $t_9\zeta_1$, $t_9\zeta_9$) and increases from $2.6 \times 10^{15} \text{ cm}^{-2}$ to $5.0 \times 10^{15} \text{ cm}^{-2}$ from small to large ζ for $t_{\text{wu}} = t_1$ (panels $t_1\zeta_1$, $t_1\zeta_9$). This trend is also apparent for other molecules including methyl formate and dimethyl ether. Figure 7 shows these trends for a selection of molecules in source NGC 6334 IRS 1; within each panel, the column density for a particular molecule is plotted for each model, starting with each cosmic-ray ionization model using $t_{\text{wu}} = t_1$ and finishing with the $t_{\text{wu}} = t_9$ models. The trend of increasing molecular column densities with increasing t_{wu} values continues to t_{wu} values around the $t_5 - t_4$ range, after which the trend reverses, as described above. However, the turnover in the trend varies somewhat depending on the molecule considered.

For most molecules, N_{tot} is also sensitive to t_{wu} changes. For instance, the N_{tot} values for methyl formate, ethanol, dimethyl ether, formic acid, and formamide increase significantly for

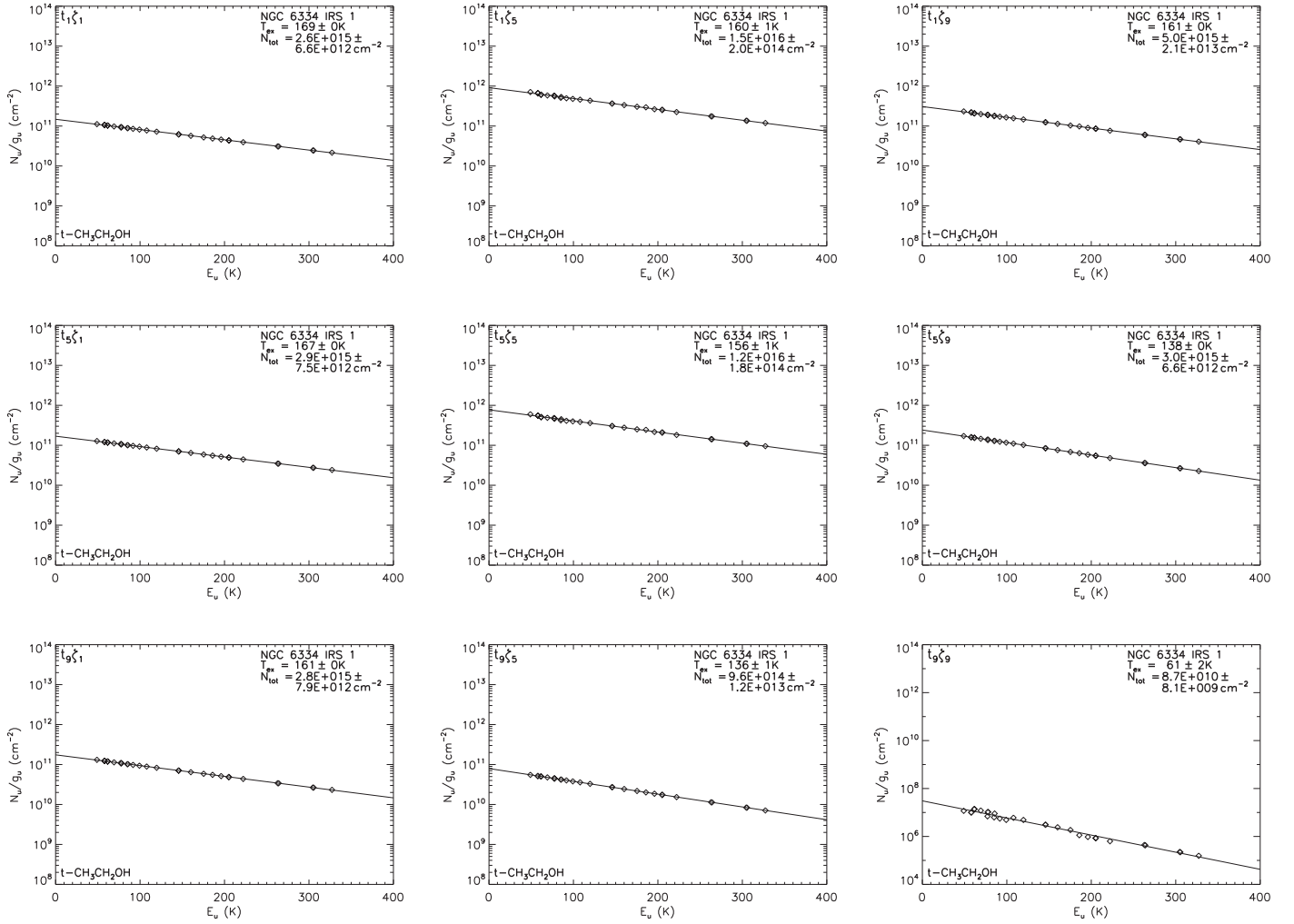


Figure 6. Select population diagrams of ethanol for source NGC 6334 IRS 1. Data points have been corrected for optical depth. Data points are not corrected for non-LTE emission.

small t_{wu} , for any single value of ζ . Figure 7 illustrates this trend for methyl formate and dimethyl ether. The N_{tot} values for a couple molecules including ketene and methyl cyanide tend to increase for medium t_{wu} (Figures 7(c)–(d)).

Trends in the excitation temperatures, T_{ex} , obtained from the population diagrams are less dependent on t_{wu} , but temperatures generally decrease for increasing ζ . Ethanol in source NGC 6334 IRS 1 (Figure 6) exemplifies this trend as its T_{ex} decreases from 169 to 161 K for $t_{\text{wu}} = t_1$, from 167 to 138 K for $t_{\text{wu}} = t_5$, and from 161 to 61 K for $t_{\text{wu}} = t_9$, with increasing ζ . Although several molecules do exhibit strong T_{ex} changes with different t_{wu} for a particular source, the behavior is mostly inconsistent between sources, and, in many cases, for low ζ values the excitation temperatures show little variation with t_{wu} . For example, T_{ex} of ethanol decreases for large t_{wu} for NGC 6334 IRS 1 and W33A but is essentially static across different t_{wu} for NGC 7538 IRS 1 and W3(H₂O) except for very high ζ . Figure 8 (panels (a) and (b)) highlights this inconsistency for ethanol in sources NGC 6334 IRS 1 and NGC 7538 IRS 1. Ketene and isocyanic acid are the only molecules having strong, consistent trends in T_{ex} with changing t_{wu} . The temperatures of these molecules are generally greatest at intermediate t_{wu} (Figures 8(c)–(d)). Aside from these

exceptions, T_{ex} consistently decreases across the grid of models from small to large ζ .

4. Comparison with Observations

While it is possible to compare column densities and excitation temperatures obtained from the spectral models directly with those derived from observations for individual molecules, the determination of the overall best model to match the observations of all molecules toward a specific source, based on N_{tot} and T_{ex} , is more challenging. Instead, rather than lend the column density and excitation temperature of each molecule some artificial weight, here we concentrate on how well the models reproduce each individual observed emission line, regardless of the molecule from which they derive. By obtaining a global best-fit parameter based on the matches between observational and modeled determinations of integrated line intensities, the best-fitting model for each source is obtained, allowing ζ and t_{wu} in turn to be constrained.

In this comparison of simulated integrated intensities with those observed by B07, we exclude several lines from the analysis that may adversely affect the fit. Observed transitions of excited states including those of gauche ethanol and higher vibrational levels are discarded because our chemical model

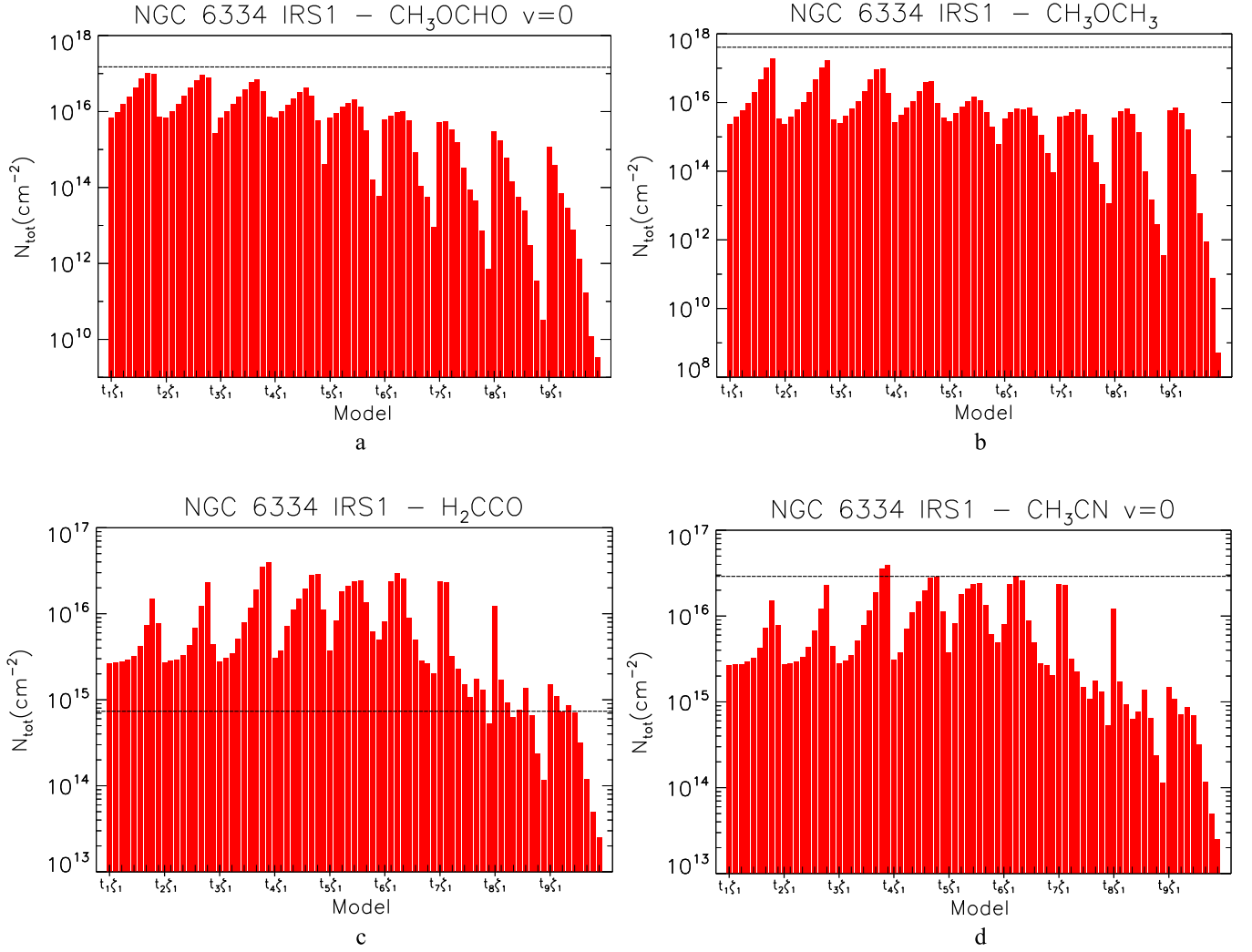


Figure 7. Source-averaged column densities (N_{tot}) for methyl formate (panel (a)), dimethyl ether (panel (b)), ketene (panel (c)), and methyl cyanide (panel (d)), obtained with each chemical model as applied to source NGC 6334 IRS 1. ζ increases from ζ_1 to ζ_9 going from left to right across the figure for each t_{w} . The dashed lines in panels (a)–(d) correspond to the measured values $N_{\text{tot}} = 1.2 \times 10^{17} \text{ cm}^{-2}$, $N_{\text{tot}} = 5.8 \times 10^{17} \text{ cm}^{-2}$, $N_{\text{tot}} = 7.4 \times 10^{14} \text{ cm}^{-2}$, and $N_{\text{tot}} = 2.9 \times 10^{16} \text{ cm}^{-2}$, respectively (B07).

computes ground-state fractional abundances only. Observed blended lines are discarded to best suit the pure spectrum treatment employed in the simulation. Integrated intensities for which upper limits are cited are also excluded to avoid uncertainty in the comparison. Finally, lines that are simulated to be optically thick are eliminated on the basis that their integrated intensities reflect only lower limits on true emission intensities and thus may skew the fit.

A few molecules observed by B07 are excluded from the analysis entirely, due to either poor or suspect model results (discussed below, in Section 5.3). Formic acid is discarded because recent literature indicates that its gas-phase chemistry may be incorrect in our model (Alvarez-Idaboy et al. 2001; Ocaña et al. 2017; Zanchet et al. 2018). In particular, the 1:50 branching ratio of Reactions (6a) to (6b) is likely too high (see Section 3.1.3). Accordingly, formic acid abundances are overproduced by a few orders of magnitude in most models. Also, the modeled integrated intensities of formaldehyde compare poorly with the observed value for all sources. For example, the observed integrated intensity for the $3_{1,2}-2_{2,1}$ transition is reported to be 57 K km s^{-1} for source NGC 6334 IRS 1; however, most models give a result that is greater than 500 K km s^{-1} . The modeled results for the

other sources are also too high by a similar magnitude. Consequently, formaldehyde is excluded on the basis of a uniformly poor match. Formamide is also excluded, due to it being overproduced and having optically thick emission in the models. The results for these molecules indicate that their chemistry is incorrect in our models and are not therefore appropriate to compare with observations.

Having eliminated poor lines and molecules, we compare qualifying integrated intensity data with corresponding observed data using the confidence of agreement treatment introduced by Garrod et al. (2007), which was originally used by those authors to compare fractional abundances. In the present treatment, the confidence of agreement, κ_i , for a pair of simulated and observed integrated intensities, $I_i = \int T_{B,i}(\nu) d\nu$, for line i is defined using the complimentary error function:

$$\kappa_i = \frac{\text{erfc}[|\log_2(I_{i,\text{mod}}) - \log_2(I_{i,\text{obs}})|]}{\sqrt{2}}. \quad (19)$$

In this treatment, the value of κ_i ranges from 1 to 0, corresponding to a good or a poor match, respectively. The final matching parameter, κ , is simply the mean average of κ_i for all i lines observed for the source in question. Because the

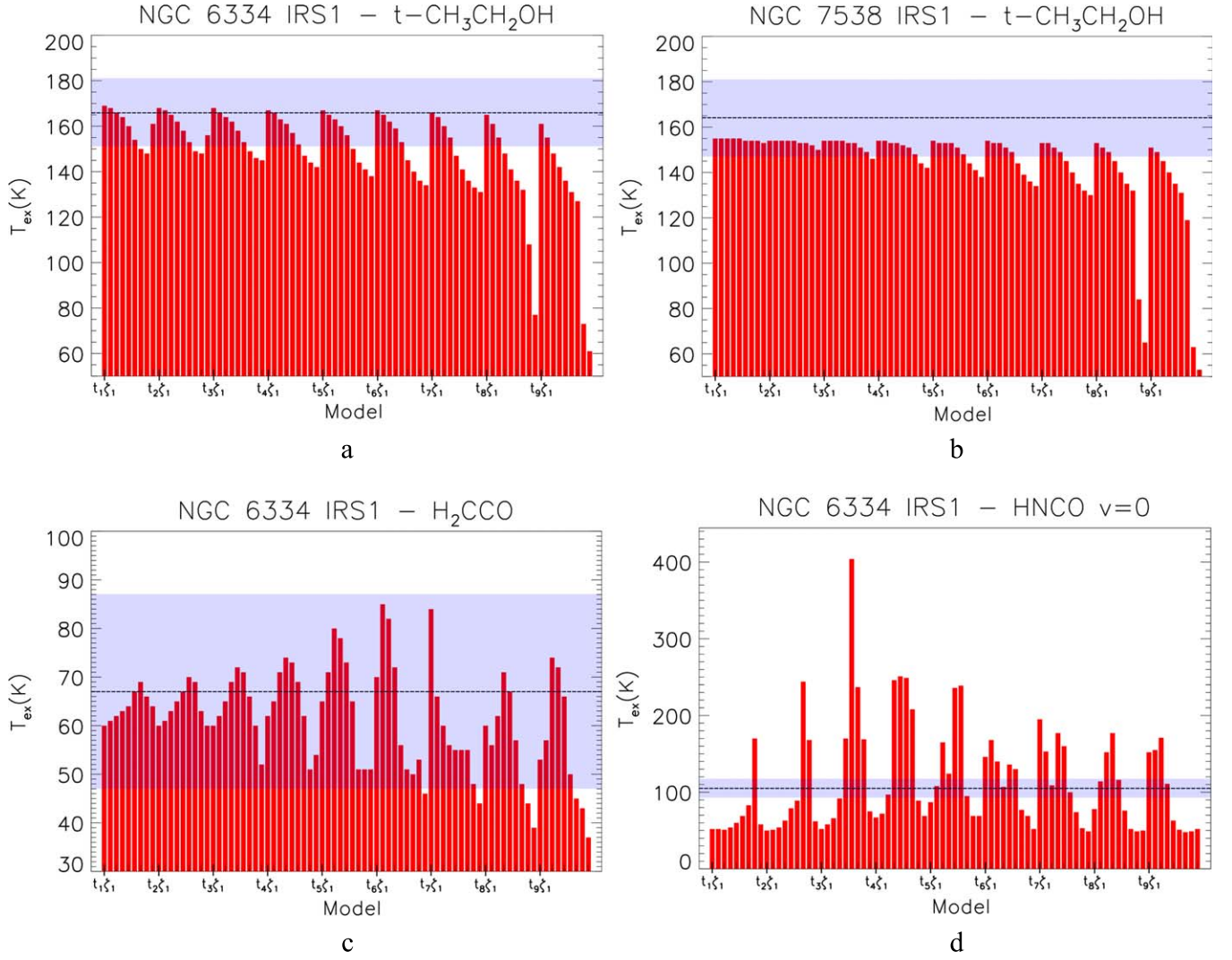


Figure 8. Excitation temperatures (T_{ex}) obtained with each chemical model for a selection of molecules and sources. Results are shown for ethanol in NGC 6334 IRS 1 (panel (a)), for ethanol in NGC 7538 IRS 1 (panel (b)), for ketene in NGC 6334 IRS 1 (panel (c)), and for isocyanic acid in NGC 6334 IRS 1 (panel (d)). The dashed lines and blue rectangles in panels (a)–(d) correspond to measured T_{ex} and uncertainties of $T_{\text{ex}} = 166 \pm 15$ K, $T_{\text{ex}} = 164 \pm 17$ K, $T_{\text{ex}} = 67 \pm 20$ K, and $T_{\text{ex}} = 105 \pm 12$ K, respectively (B07).

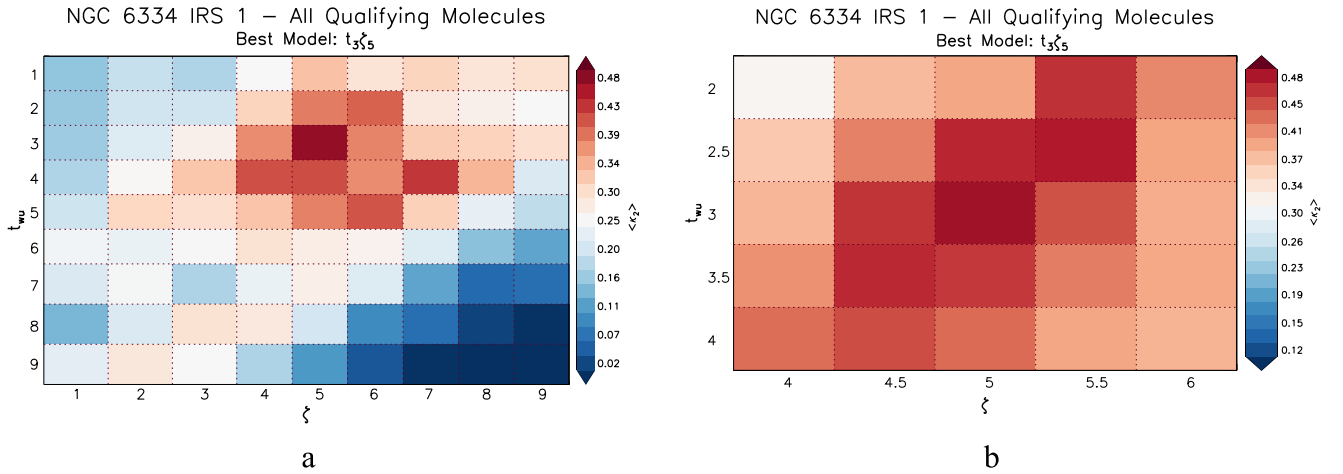


Figure 9. Comparison of modeled and observed integrated intensities for source NGC 6334 IRS 1 using the κ analysis. Higher (redder) values of κ indicate a better match. Formic acid, formamide, and formaldehyde are omitted from the analysis. Panel (a) features the results for all chemical models. Panel (b) features the results of fine grid models. The additional models in the fine grid are denoted as half-integer values of the original timescales and cosmic-ray ionization rates.

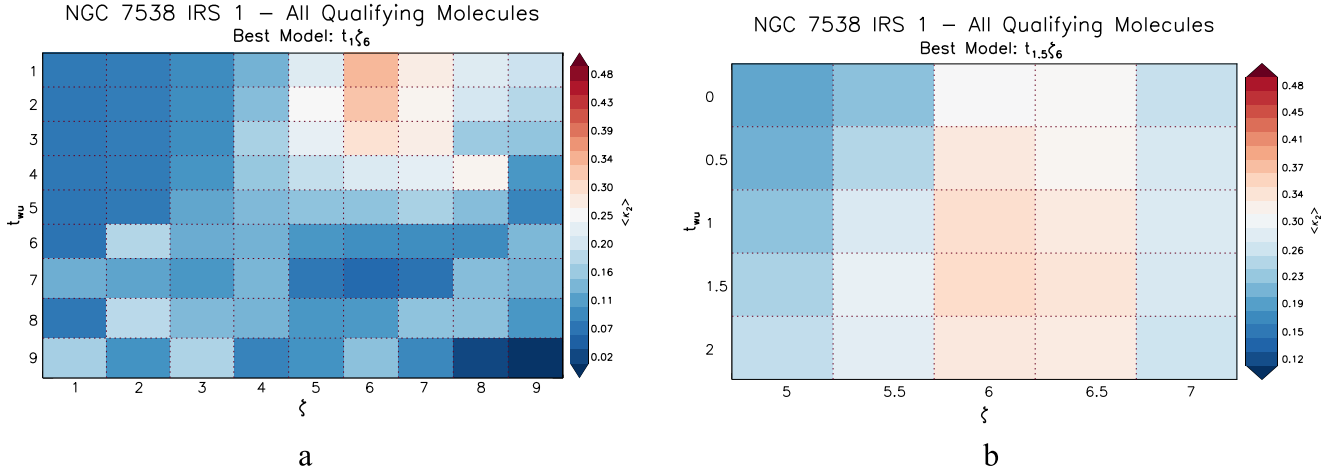


Figure 10. Comparison of modeled and observed integrated intensities for source NGC 7538 IRS 1. As per Figure 9.

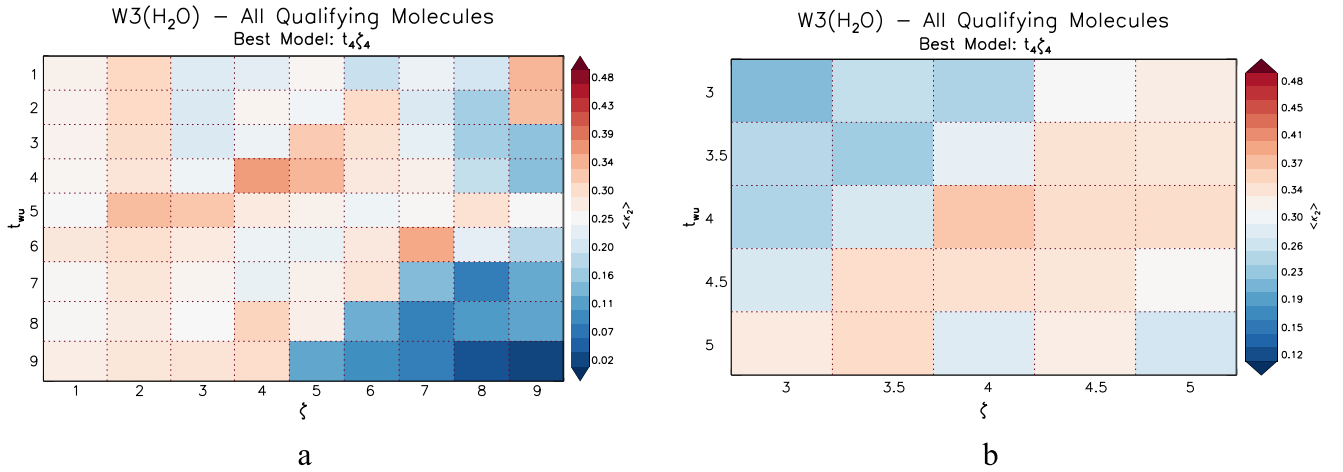


Figure 11. Comparison of modeled and observed integrated intensities for source W3(H₂O). As per Figure 9.

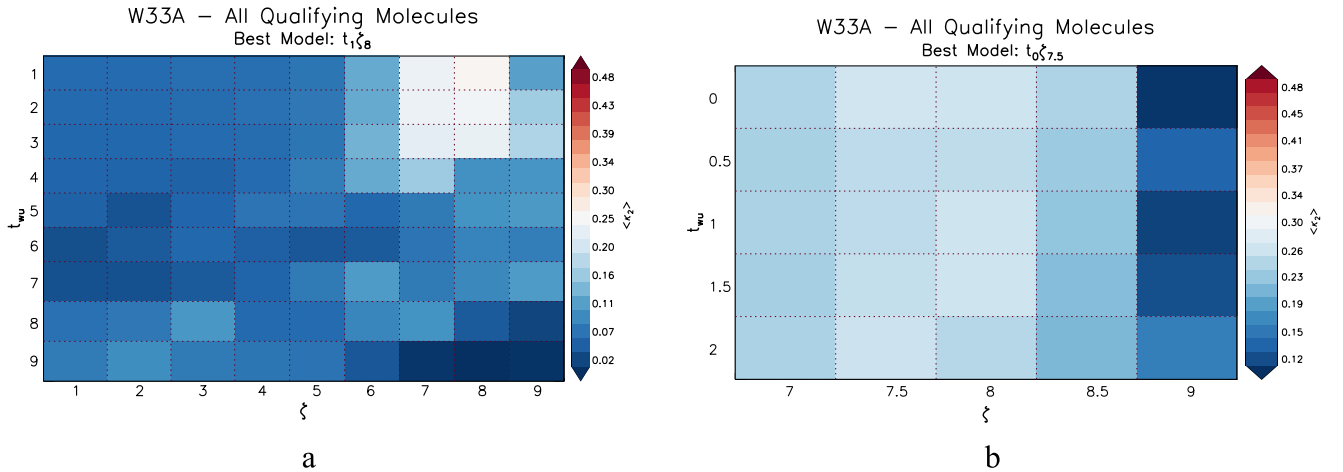


Figure 12. Comparison of modeled and observed integrated intensities for source W33A. As per Figure 9.

value of κ_i for an arbitrarily bad match approaches zero, this ensures that it does not unduly affect the overall match. Thus, this method rewards success but does not punish failure beyond some scale distance from the “true value.” This scale distance corresponds to the models diverging by a factor of two, up or down, as compared to the observed integrated intensity of the line. We choose log base-2 instead of base-10 to produce a

tolerance that is more sensitive to small changes in the comparison.

Figures 9–12 illustrate the variation in the agreement parameter, κ , for each source, using each model in the grid. Red colors indicate a better match, while blue indicates a worse match. The same color scale is used to map κ in each plot, so that the quality of the match may be compared between

Table 4
Fine Fluence Grid Parameters

Warm-up Timescale		Cosmic-Ray Ionization Rate	
Notation	Time to Reach 200 K (yr)	Notation	$\zeta(\text{s}^{-1})$
t_0	1.56×10^3	$\zeta_{3.5}$	1.84×10^{-17}
$t_{0.5}$	2.21×10^3	$\zeta_{4.5}$	3.68×10^{-17}
$t_{1.5}$	4.42×10^3	$\zeta_{5.5}$	7.35×10^{-17}
$t_{2.5}$	8.84×10^3	$\zeta_{6.5}$	1.47×10^{-16}
$t_{3.5}$	1.77×10^4	$\zeta_{7.5}$	2.94×10^{-16}
$t_{4.5}$	3.54×10^4	$\zeta_{8.5}$	5.88×10^{-16}

sources. The height and width of each colored rectangle scale to the logarithmic spacing between models.

In order to constrain the ζ and t_{wu} values beyond the resolution of the main model grid, refined grids were created for each source using the best-fit model as the central value. Taking the original 3×3 subgrid of models surrounding the best-fit model, the resolution is doubled to generate a 5×5 fine grid featuring two additional timescales and values of ζ , corresponding to 16 new chemical models, each denoted with half-integer values for t and ζ . For example, $t_{5.5}$ is the timescale corresponding to the logarithmic midpoint between t_5 and t_6 . The new refined grid parameters are listed in Table 4. The confidence of agreement treatment is then reiterated for the fine grid to give a new best-fit model with improved resolution. The results of the analytical treatment for the four sources surveyed are summarized in the following subsection. The best-fit results and constraints on ζ and t_{wu} are summarized in Table 5.

4.1. NGC 6334 IRS 1

Model comparisons for source NGC 6334 IRS 1 are presented in Figure 9. For the full grid (panel (a)), κ values are generally greater than 0.15 (an average agreement between modeled and observed integrated intensities within a factor of about 2), and the best agreement lies roughly in the upper middle with values greater than 0.30 (an average within a factor of about 1.7). For both the full and fine grid (panel (b)), the best fit occurs for model $t_3\zeta_5$, with $\kappa = 0.471$ (an average within a factor of about 1.4), and gives $\zeta = 5.20 \times 10^{-17} \text{ s}^{-1}$.

4.2. NGC 7538 IRS 1

Model comparison results for source NGC 7538 IRS 1 are presented in Figure 10. For the full grid (panel (a)), κ values are generally greater than 0.05 (an average within a factor of about 2.6), and the best agreement lies in the upper middle right with values greater than 0.23 (an average within a factor of about 1.8). The best-fit models of the full and fine grid (panel (b)) are $t_1\zeta_6$ ($\kappa = 0.334$) and $t_{1.5}\zeta_6$ ($\kappa = 0.337$), respectively (both an average within a factor of about 1.6). Using the fine grid result, $\zeta = 1.04 \times 10^{-16} \text{ s}^{-1}$.

4.3. W3(H₂O)

Model comparison results for source W3(H₂O) are presented in Figure 11. For the full grid (panel (a)), κ values are mostly greater than 0.15 (an average within a factor of about 2.0); however, there is no apparent region of the grid where the agreement converges to produce best results (discussed in Section 5.2). Nonetheless, there are a few points in parameter space that give good matches. For both the full and fine grid

Table 5
Summary of Best-fit Results

Source	Best Model	κ	Fit to $\zeta (\text{s}^{-1})$	Fit to $t_{\text{wu}} (\text{yr})$
NGC 6334 IRS 1	$t_3\zeta_5$	0.471	5.20×10^{-17}	1.25×10^4
NGC 7538 IRS 1	$t_{1.5}\zeta_6$	0.337	1.04×10^{-16}	4.42×10^3
W3(H ₂ O)	$t_4\zeta_4$	0.357	2.60×10^{-17}	2.50×10^4
W33A	$t_0\zeta_{7.5}$	0.261	2.94×10^{-16}	1.56×10^3

(panel (b)), the best fit occurs for model $t_4\zeta_4$, with $\kappa = 0.357$ (an average within a factor of about 1.6), and gives $\zeta = 2.60 \times 10^{-17} \text{ s}^{-1}$.

4.4. W33A

Model comparison results for source W33A are presented in Figure 12. For the full grid (panel (a)), κ values are low across most of the grid, as they do not exceed 0.10 (an average within a factor of about 2.2) for the majority of the models. There is, however, a well-defined region of best fit in the upper right corner with κ values greater than 0.20 (an average within a factor of about 1.9). The best-fit models of the full and fine grid (panel (b)) are $t_1\zeta_8$ ($\kappa = 0.259$) and $t_0\zeta_{7.5}$ ($\kappa = 0.261$), respectively (both an average within a factor of about 1.7). Using the fine grid result, $\zeta = 2.94 \times 10^{-16} \text{ s}^{-1}$.

5. Discussion

The models presented here consider the dependence of COM chemistry in hot cores on the complementary parameters of cosmic-ray ionization rate and warm-up timescale. A large proportion of the parameter space appears to provide a potentially acceptable set of results to match observed COM abundances, although the models with the highest nominal cosmic-ray fluence (i.e., the product of ζ and t_{wu}) demonstrate a catastrophic destruction of gas-phase molecules, in spite of significant COM production on the dust grains.

The general behavior shown by the models is that, with increasing ζ , CRPD of major ice constituents generates more radicals, which react to produce greater abundances of COMs in ice mantles, while large t_{wu} lead to diminished abundances. Although formation reactions tend to elevate abundances, they are only effective for a small fraction of a molecule's lifetime in the ice, prior to desorption. At temperatures above about 40 K, destruction by H abstraction and CRPD mechanisms predominates. As ζ increases, abundances are larger for small t_{wu} (Figures 2–5), somewhat smaller for medium t_{wu} , and considerably smaller for large t_{wu} at the time of desorption. In the models with the smallest ζ values, variation of t_{wu} has little effect on COM abundances.

Most COMs considered in this study are first formed on grains and then desorb at a characteristic temperature. Therefore, higher ice abundances correspond to larger gas-phase peaks upon desorption, and lower ice abundances result in smaller gas-phase peaks for these species. However, the effect of increasing ζ results in greater destruction of gas-phase material via ion–molecule protonation schemes and is especially strong for large t_{wu} (Figures 2–5). For these conditions, gas abundances become severely diminished at the desorption temperature. For small t_{wu} , abundances are also diminished with increasing ζ (panels $t_1\zeta_1$, $t_1\zeta_5$, $t_1\zeta_9$), although they survive to higher temperatures, since the time for which destruction can occur is very brief. Thus, abundances are larger for the

remainder of the warm-up relative to large t_{wu} . Abundance trends of species having significant gas-phase formation routes are somewhat variable, though they are also generally diminished at large t_{wu} and high ζ .

To summarize these trends, large ζ leads to production of COMs on grains especially at low temperatures in the warm-up, while at higher temperatures these conditions also tend to destroy COMs once their formation has ceased. Large t_{wu} allow COMs to accumulate at low temperatures, but they are also destroyed at high temperatures. Intermediate values of t_{wu} provide a balance between early formation and late destruction of ices. Since most molecules lack significant gas-phase formation pathways, they are destroyed through protonation and dissociative recombination after they desorb. This effect is amplified for large t_{wu} . The trends seen in the fractional abundances are similarly carried through to the column densities calculated for COMs using the radiative transfer model.

According to these trends, rapidly evolving sources (i.e., those with short warm-up timescales) may lack significant formation or processing of dust-grain ice mantles, which corresponds to lower gas-phase abundances in warm regions. Alternatively, more slowly evolving sources would develop chemically processed grain mantles in their outer envelopes, but the constituents would likely be diminished in warmer regions. We may infer that sources with intermediate warm-up timescales and elevated ζ (on the order of 10^{-16} s^{-1}) provide a balance to these conditions and possess the greatest and most widespread chemical richness on grains and in the gas phase. It should be noted that the warm-up timescale corresponds to the physical/chemical evolution of a parcel of gas/dust but does not necessarily correspond to the physical age of the source as a whole. The warm-up stage in theory reflects both the increase in luminosity of the protostar and the gradual decrease in radial distance of the gas parcel from the source. The warm-up timescale therefore should have more to do with the overall mass accretion rate of the protostar than with its age.

5.1. General Trends in Simulated Column Densities and Excitation Temperatures

Similar trends are seen in the column densities of COMs calculated using our LTE radiative transfer and beam convolution model as are obtained for the peak fractional abundances in the models. Thus, for the COMs modeled here at least, this indicates that observed column density trends may be taken as a good indicator of the underlying chemical behavior. As may be seen in Figure 7, for short warm-up timescales, increasing ζ leads to greater COM column densities, whereas for long warm-up timescales, higher zeta leads to greater destruction of the COMs. Although there is some degeneracy seen between models of the same nominal cosmic-ray fluence, e.g., models $t_3\zeta_1$ and $t_2\zeta_2$, in general the models with the same fluence cannot be said to show the same behavior, although this varies for each molecule.

In all of the sources modeled here, T_{ex} for many molecules increases consistently across the model grid from large to small ζ (e.g., Figures 8(a)–(b)). This behavior emerges from the fact that large ζ destroys molecules in the gas phase more rapidly; rapid destruction in the gas phase prohibits the survival of those molecules to later times and thus to higher temperatures. However, considering the large errors in the observational determinations of T_{ex} by B07, which is typical for hot-core

sources, the models show a much broader agreement with observations based on excitation temperature than on column density.

Such variation as there is in the simulated T_{ex} values appears to reflect a balance between the spatial region of emission (which depends on both the source density profile and the molecular fractional abundance) and the beam size, rather than the characteristic desorption temperature or temperature of greatest abundance in the gas. For example, ethanol ($\text{C}_2\text{H}_5\text{OH}$) desorbs from the dust grains at $\sim 110 \text{ K}$, but its T_{ex} values are consistently higher. The centrally peaked density and temperature structure has a strong effect on the region of strongest emission. T_{ex} is typically in the range of about 130–170 K for NGC 6334 IRS 1 (Figure 8(a)). Furthermore, there are several models for which the gas-phase fractional abundances of ethanol remain large until the warm-up stage ends, at 400 K (e.g., Figure 2, panels $t_1\zeta_1$, $t_1\zeta_5$, $t_5\zeta_1$), but for which T_{ex} is not close to 400 K. This is due to the fact that, at the point in the radial profile where a temperature of 110 K is attained, the emission is extended but the gas density is somewhat low, and for the gas at 400 K, the gas density is high but the emission is compact. Instead, T_{ex} is intermediate to these values and represents a position where the gas density and spatial extent of the emission are both sufficiently high to dominate the line intensity. In fact, for the beam sizes simulated in these models, all of this emission is well within the telescope beam.

The agreement of modeled with observed values of T_{ex} and, in particular, N_{tot} is mixed. For source NGC 6334 IRS 1, for example, simulated values for ethanol agree well with observations, whereas those for dimethyl ether do not. B07 determined ethanol to have $N_{\text{tot}} = 1.9 \times 10^{16} \text{ cm}^{-2}$ and $T_{\text{ex}} = 166 \pm 14 \text{ K}$ for this source. The best-fit model ($t_3\zeta_5$) from the present grid produces $N_{\text{tot}} = 1.4 \times 10^{16} \text{ cm}^{-2}$ and $T_{\text{ex}} = 158 \pm 1 \text{ K}$, which agrees well with the observations. However, observed N_{tot} and T_{ex} for dimethyl ether are $5.8 \times 10^{17} \text{ cm}^{-2}$ and $241 \pm 35 \text{ K}$, respectively, whereas our best-fit model gives $N_{\text{tot}} = 2.0 \times 10^{16} \text{ cm}^{-2}$ and $T_{\text{ex}} = 105 \pm 0 \text{ K}$. Furthermore, Table 6 cites a comparison among best-fit model and observed values of N_{tot} and T_{ex} of all molecules for each source. Modeled values that agree well with the observations are cited in boldface. In particular, we consider any pair of modeled and calculated values of N_{tot} that lies within an order of magnitude to be in good agreement. Similarly, any pair of T_{ex} values that lies within the range of cited uncertainties is considered to be in good agreement. In general, modeled values of N_{tot} that are in good agreement with observed values are underproduced.

Thus, although the models are differentiated strongly for a molecule, it is quite possible that there exist systematic errors in the chemical treatment that underproduces it. For example, gas-phase COMs are destroyed by protonation ions in our models. However, other gas-phase molecules with high proton affinities such as ammonia may neutralize a significant fraction of these ions (Taquet et al. 2016). Accordingly, COM gas-phase abundances may be higher, though we do not currently account for such processes. Also, our model assumes an equal efficiency of UV photodissociation in the solid and gas phases. However, Kalváns (2018) suggests that solid-phase photodissociation is only about one-third as efficient as gas-phase photodissociation. This may result in some systematic error in modeling surface abundances; however, it is difficult to speculate how this error would propagate in the context of

Table 6
Comparison of Calculated Column Densities and Excitation Temperatures with Observed Values for Each Source

Molecule	NGC 6334 IRS 1				NGC 7538 IRS 1			
	$N_{\text{tot}}^{\text{mod}}$ (cm^{-2})	$T_{\text{ex}}^{\text{mod}}$ (K)	$N_{\text{tot}}^{\text{obs}}$ (cm^{-2})	$T_{\text{ex}}^{\text{obs}}$ (K)	$N_{\text{tot}}^{\text{mod}}$ (cm^{-2})	$T_{\text{ex}}^{\text{mod}}$ (K)	$N_{\text{tot}}^{\text{obs}}$ (cm^{-2})	$T_{\text{ex}}^{\text{obs}}$ (K)
H ₂ CO*	1.3(17)	193 ^a	2.5(16)	87 ^a
CH ₃ OH	1.8(18)	135 ± 2	9.7(17)	178 ± 10	2.0(16)	137 ± 3	1.2(17)	156 ± 10
C ₂ H ₅ OH	1.4(16)	158 ± 1	1.9(16)	166 ± 15	2.4(14)	154 ± 0	5.7(15)	164 ± 17
HNCO	8.8(14)	170 ± 73	4.3(15)	105 ± 12	2.8(13)	52 ± 2	2.3(15)	278 ± 88
NH ₂ CHO*	1.6(17)	132 ± 2	7.4(14)	166 ± 29	1.9(15)	123 ± 5	5.7(14)	164 ± 28
CH ₃ CN	4.9(14)	188 ± 188	2.9(16)	170 ± 13	4.5(12)	145 ± 145	<8.2(15)	[218]
C ₂ H ₅ CN	3.6(14)	164 ± 1	5.1(15)	92 ± 3	3.7(12)	150 ± 0	<9.2(14)	[96]
HCOOCH ₃	3.8(16)	141 ± 1	1.2(17)	144 ± 7	9.7(14)	134 ± 1	1.4(16)	134 ± 8
CH ₃ OCH ₃	2.0(16)	105 ± 0	5.8(17)	241 ± 35	1.7(15)	91 ± 0	1.6(16)	[130]
CH ₂ CO	7.9(15)	72 ± 15	7.2(14)	67 ± 20	6.6(14)	49 ± 4	9.7(13)	37 ± 4
CH ₃ CHO	<1.2(14)	[37.5]	2.1(17)	96 ± 10	2.8(13)	18 ± 5
HCOOH*	4.3(15)	110 ± 2	4.9(14)	63 ± 12	2.2(14)	52 ± 2	9.8(13)	73 ± 12
C ₃ H ₄	4.2(15)	104 ± 2	5.2(15)	63 ± 12	5.6(14)	67 ± 3	8.4(14)	58 ± 10
	W3(H ₂ O)				W33A			
	$N_{\text{ex}}^{\text{mod}}$ (cm^{-2})	$T_{\text{ex}}^{\text{mod}}$ (K)	$N_{\text{tot}}^{\text{obs}}$ (cm^{-2})	$T_{\text{ex}}^{\text{obs}}$ (K)	$N_{\text{ex}}^{\text{mod}}$ (cm^{-2})	$T_{\text{ex}}^{\text{mod}}$ (K)	$N_{\text{tot}}^{\text{obs}}$ (cm^{-2})	$T_{\text{ex}}^{\text{obs}}$ (K)
...	1.8(17)	181 ^a	5.4(16)	88 ^a
5.4(17)	133 ± 2		1.0(18)	139 ± 8	3.8(15)	144 ± 8	2.0(17)	259 ± 16
2.5(15)	158 ± 2		8.4(15)	129 ± 16	9.1(13)	155 ± 0	4.7(15)	122 ± 16
1.6(14)	175 ± 72		4.9(15)	147 ± 24	7.4(12)	51 ± 1	6.6(15)	85 ± 8
3.3(16)	132 ± 1		1.3(15)	71 ± 7	3.4(14)	124 ± 5	2.1(15)	40 ± 13
6.6(14)	125 ± 9		7.0(15)	196 ± 14	2.3(12)	118 ± 5	2.7(16)	278 ± 44
1.2(14)	161 ± 1		4.5(15)	94 ± 16	5.0(11)	152 ± 1	<2.1(15)	[96]
6.0(15)	142 ± 1		5.2(16)	109 ± 7	3.3(14)	134 ± 0	2.5(16)	112 ± 5
3.1(15)	108 ± 1		1.5(17)	94 ± 5	1.2(15)	91 ± 0	2.7(16)	43 ± 7
3.7(15)	64 ± 12		1.1(14)	54 ± 8	1.6(14)	61 ± 1	6.3(13)	45 ± 7
4.8(16)	99 ± 6		3.5(13)	16 ± 3	<3.0(13)	[37.5]
1.6(15)	88 ± 10		1.5(14)	189 ± 108	8.8(13)	57 ± 1	1.3(14)	38 ± 6
1.3(15)	103 ± 2		1.5(15)	82 ± 15	5.1(14)	63 ± 2	1.3(15)	40 ± 6

Note. Here mod refers to values of N_{tot} and T_{ex} calculated using the best-fit model for each source (see Table 5); obs refers to values of N_{tot} and T_{ex} observed by B07. Molecules marked with an asterisk are those omitted from the analysis to find best-fit models (see Section 4). No calculation has been made for entries marked with ellipses. Values of T_{ex} marked with *a* are taken from van der Tak et al. (2000). Entries in brackets are assumed values (see B07 for details). Calculated and observed pairs of N_{tot} and T_{ex} that agree well are cited in boldface.

cosmic-ray ionization. Inaccuracies in the physical treatment are also possible. In particular, the density and temperature profiles that we use incorporate no smaller-scale or asymmetric structure, while more recent observations of, for example, NGC 6334 IRS 1 with ALMA indicate its presence (Brogan et al. 2018).

5.2. Constraints on ζ and t_{wu}

Based on a match parameter that directly compares the simulated and observed line-integrated intensities for a range of COMs (thus removing the need to compare column densities and excitation temperatures directly), we determined the best-matching model for each of the four observational sources, NGC 6334 IRS 1, NGC 7538, W33A, and W3(H₂O); see Table 5. These best-fit models correspond to a particular value of the cosmic-ray ionization rate and warm-up timescale. It is immediately apparent that the ζ values obtained are uniformly greater than the canonical value, $1.3 \times 10^{-17} \text{ s}^{-1}$, while the warm-up timescales are uniformly shorter than any of the values previously used in our hot-core models (e.g., Garrod 2013; Belloche et al. 2017). The best-fit values of ζ range from around 2 to 20 times the canonical cosmic-ray ionization rate. The warm-up timescales are around 4–32 times shorter than the *fast* value of $5 \times 10^4 \text{ yr}$ used in the past. These timescales of around 10^3 – 10^4 yr indicate that there would be little time for ion–molecule processes to destroy gas-phase COMs, almost regardless of cosmic-ray ionization rate. The high ζ values favored by the fits are then free to produce high grain-surface abundances of COMs.

Although the constraints on ζ are lower than those determined toward the Galactic center (e.g., Oka et al. 2005; Le Petit et al. 2016), they are not inconsistent, as those observational values are more reflective of diffuse cloud conditions. Cosmic rays are attenuated by intervening dust as they pass through a source (Padovani et al. 2009, 2018; Rimmer et al. 2012). This implies that although we model ζ as 10^{-17} to 10^{-16} s^{-1} , these values only reflect conditions present within the sources. The values toward the edges are likely larger and could be on the order of 10^{-15} to 10^{-14} s^{-1} . The method of finding best-fit models presented here, based on COM abundances, provides means with which to estimate—albeit indirectly—the cosmic-ray ionization rate most appropriate to the dense conditions found in hot-core sources.

Referring to Table 5, the match parameter, κ , is greatest for NGC 6334 IRS 1 and lowest for W33A (with values of 0.471 and 0.261, respectively), indicating that the modeled integrated intensities of surveyed molecules have comparatively better agreement for NGC 6334 IRS 1 than W33A. In particular, methanol, ethanol, methyl formate, and dimethyl ether agree well for several models across the grid for NGC 6334 IRS 1 but have very poor agreement across the grid for W33A. The discrepancy could be attributed to the fact that NGC 6334 IRS 1 is observed to be chemically rich, whereas W33A is chemically poor (also see Section 5.4). B07 note that NGC 7538 IRS 1 is also chemically poor, and it achieves the second-lowest κ value in our comparison (0.337). Alternatively, the temperature and density profiles that we use for these sources may not be as good of a representation of reality as those for NGC 6334 IRS 1 and W3(H₂O).

Model comparison results for source W3(H₂O) show that best-matching models do not seem to converge in one region of the grid (Figure 11(a)). The fit is patchy, and the best matches

are spread across different regions of parameter space. The three best matches occur for models $t_4\zeta_4$, $t_6\zeta_7$, and $t_1\zeta_9$. This arises from individual molecules having their own best fits to observed integrated intensities in these different regions. For example, C₃H₄, dimethyl ether, and isocyanic acid agree best in the $t_4\zeta_4$ region, ethyl cyanide agrees well in both the $t_4\zeta_4$ and $t_6\zeta_7$ regions, and ethanol agrees well in both the $t_6\zeta_7$ and $t_1\zeta_9$ regions. The mixed agreement could be due to the fact that W3(H₂O) is a protobinary system rather than a single core (Chen et al. 2006), and the respective cores could possess disparate chemical compositions. Indeed, the other three sources are reported to consist of multiple fragments or substructures (Caproni et al. 2002; Beuther et al. 2013; Izquierdo et al. 2018), though they may all be consistent in age and composition, or dominated by a single component. Though it is unlikely for the components of W3(H₂O) to originate from different clouds, it could be that they vary in age and thus account for the chemical differences. If this is the case, then our modeling approach could provide an indirect means of chemically resolving such sources into multiple components.

To provide an alternative test for the rate of cosmic-ray-induced ionization provided by the best-fit models, we plot (Figure 13, panel (a)) the best-fit ζ as a function of total hydrogen column density, based on a simple integration of the gas density profiles provided by van der Tak et al. (2000). Following the theoretical relationship between these two quantities obtained by Padovani et al. (2009), Rimmer et al. (2012), and others, they are plotted here in log-log space. The error bars on the points indicate the uncertainty in the models based on the grid resolution. The negative correlation between ζ and $N(\text{H})$ shown in Figure 13(a) agrees qualitatively with the theoretical behavior. The correlation coefficient for the best-fit line is $r = -0.87$, with the fit given by

$$\log_{10} \zeta = (-0.547 \pm 0.25) \log_{10} N(\text{H}) - (2.89 \pm 6.13). \quad (20)$$

A rough comparison between this fit and the recent calculations by Padovani et al. (2018) for dark-cloud conditions places our values a little above those authors' upper limit for ionization caused solely by external cosmic rays. This could provide evidence that there is some protostellar source of cosmic-ray ionization, an idea that Padovani and coworkers have also suggested. However, considering the few data points upon which our fit is based, our values would also be consistent with the upper values of ζ found by Padovani et al. (2018), without the assistance of an internal source. It is also reasonable to suggest that the values that provide the best fits to observed values could have some bias toward the earlier stages of chemical evolution, during which icy grain mantles are processed, which may be characterized by somewhat lower hydrogen column densities appropriate to this material being somewhat more extended and (relatively) diffuse. More specific modeling efforts are clearly needed that consider variable cosmic-ray ionization rates in the context of more detailed dynamical treatments. It is nevertheless encouraging that the values produced by our chemical/spectral model fits, which are otherwise unbiased with respect to total hydrogen column density, should produce the appropriate behavior for our sample of sources. This adds some further weight to the validity of the best-fit estimates for each source.

Figure 13(b) shows the warm-up timescales obtained from the best-fit models for each source, plotted against the

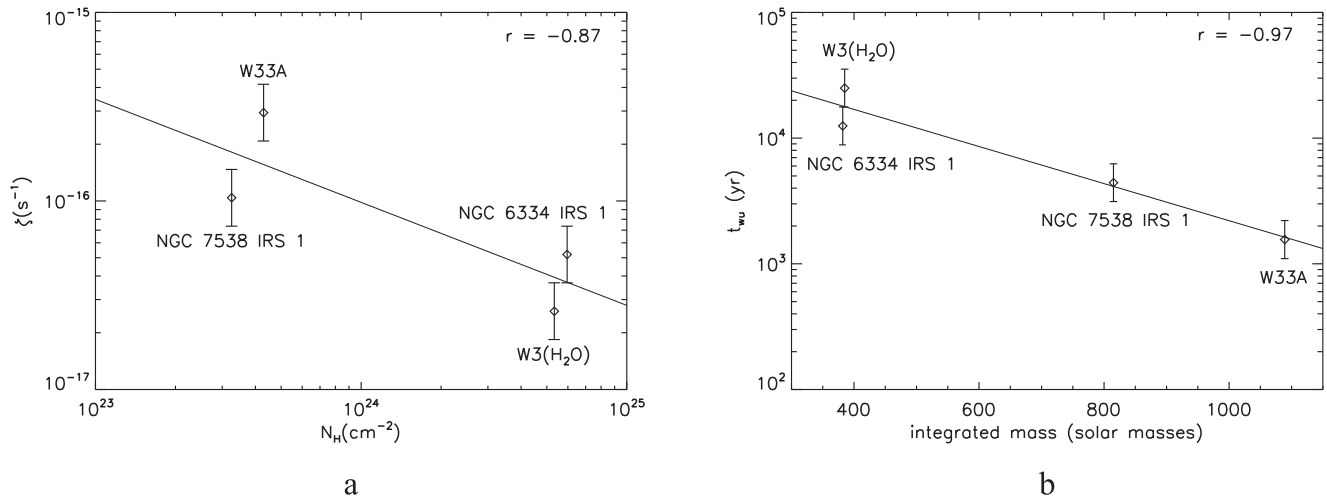


Figure 13. Relationships between ζ , t_{wu} and key physical parameters for observed sources. Panel (a) shows the best fit to ζ plotted as a function of the calculated unconvolved H column density for each source. Panel (b) shows the best fit to t_{wu} plotted as a function of stellar mass for each source. The equation of best fit is used to derive analytical expressions for the relationships among these parameters. Error bars on ζ and t_{wu} correspond to the model grid resolution.

integrated mass provided by the density profiles as determined by van der Tak et al. (2000). Here, there is an even stronger (anti)correlation ($r = -0.97$) for the log-linear best-fit line:

$$\log_{10} t_{\text{wu}} = (1.48 \pm 0.47 \times 10^{-3})M + (4.82 \pm 0.32), \quad (21)$$

where M is the integrated mass of a source in units of solar mass. Again, the clear relationship between these values adds further confidence to the general approach taken in this paper. The specific relationship in which warm-up timescales are shorter for more massive sources also makes sense, if this timescale is related to the mass accretion rate of the central protostar. The empirical relationship we find here goes in the same sense as that suggested by Viti et al. (2004), whereby more massive protostars would have shorter timescales. Their treatment was based on the protostellar luminosity function of Molinari et al. (2000), with the warm-up timescales ultimately constrained by contraction timescales. All of the sources we model here are high-mass objects; however, if this relationship holds to yet lower masses, one might expect that low-mass sources would be more strongly characterized by stronger gas-phase destruction of COMs, especially if combined with the somewhat higher cosmic-ray ionization rates that our fits suggest would be appropriate for sources with lower overall hydrogen column densities. This could manifest itself through a bias toward lower excitation temperatures in low-mass sources.

The accuracy of the above constraints may be limited by the fidelity of the temperature and density profiles used. These profiles are observationally determined best fits using continuum emission (van der Tak et al. 2000). These profiles may provide satisfactory agreement for extended regions of a source, but they fail in the compact regions where most molecular emission occurs. For example, recent ALMA surveys indicate great small-scale complexity in NGC 6334 I (Brogan et al. 2018).

5.3. Poor Chemical Matches

Our comparison with observed molecular emission omits formaldehyde, formic acid, and formamide, on the basis of uniformly poor matches with the line-integrated intensities. All

of these molecules are consistently overproduced in the models, which leads to integrated intensities that are too high for all sources. These results suggest that either the chemical or spectral modeling for these molecules is incorrect or incomplete.

The poor match of formaldehyde could be attributed to difficulty in tuning the balance between activation barriers for the reactions that form and destroy it on grains (listed in G13), which compose a part of the grain-surface chemistry network leading from CO to methanol. It is possible that either the barriers for H_2CO destruction to form CH_3O , CH_2OH , or HCO are too high, or the barriers for reformation by H abstraction from methanol are too low, or some combination thereof. However, the model results for methanol agree well with observations. Alternatively, trapping of formaldehyde in ice mantles may contribute to the poor match. If the models do not adequately account for trapping, then simulated abundances may be artificially large, in particular at low temperatures.

More likely, however, is that the radiative transfer calculations performed here are inadequate for this molecule. Only one transition of $\text{H}_2^{12}\text{C}^{16}\text{O}$ ($3_{1,2}-2_{1,1}$) out of the seven searched for by B07 was detected by those authors in the sources that are modeled here. That line should have a critical density on the order of 10^7 cm^{-3} . If the majority of the gas-phase formaldehyde is released from grains and reaches a gas-phase abundance peak at around 40 K at the radii at which that temperature is achieved, the source densities, which we calculate from the physical profiles to be on the order of 10^5 cm^{-3} , are too low to assume LTE to be valid. The paucity of formaldehyde lines at millimeter/submillimeter frequencies that have both a small-enough Einstein A-coefficient and a low-enough upper energy level to be well populated at 40 K therefore means that a non-LTE treatment is unavoidable for an accurate reproduction of observed line intensities.

On the topic of formic acid production, the gas-phase reaction between formaldehyde and OH to generate formic acid is likely incorrect. The present network takes a 1:50 branching ratio between Reactions (6a) and (6b), while Alvarez-Idaboy et al. (2001), Ocaña et al. (2017), and Zanchet et al. (2018) suggest that Reaction (6b) may be yet more dominant, due to its lower energy barrier. Consequently, formic acid abundances are artificially high. Adjusting the branching ratio accordingly may yield more

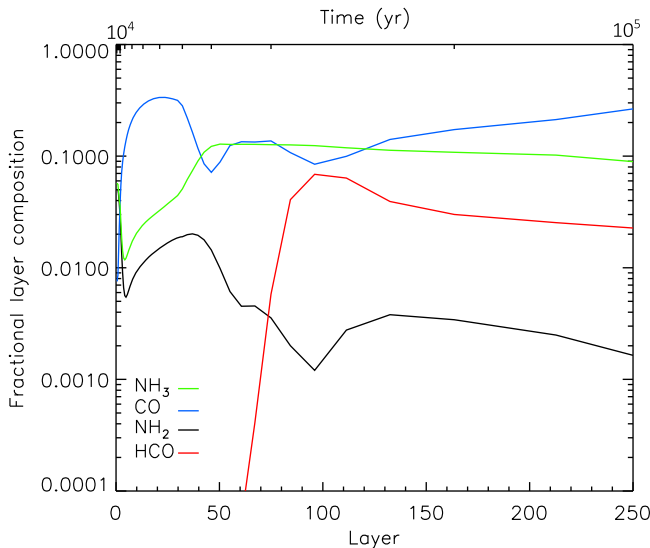


Figure 14. Ice-mantle abundances of NH_3 , CO , NH_2 , and HCO with respect to cumulative water abundances for each monolayer in a typical grain for model $t_7\zeta_3$. The model corresponds to the medium t_{wu} and standard ζ from G13.

accurate results; we leave this to future study. It should be noted that the excitation temperatures obtained by B07 for formic acid are, except for source W3(H_2O), uniformly less than 100 K, while the value for W3(H_2O), 189 ± 108 K, is still consistent with such a low value. While this behavior may be in line with the model predictions of a low-temperature component for gas-phase formic acid abundance, it would also likely place this molecule, like formaldehyde, into a regime in which the LTE assumption is not strictly valid.

Formamide is overproduced and consequently optically thick in our simulations even after omitting the formation pathway $\text{NH}_{2(\text{g})} + \text{H}_2\text{CO}_{(\text{g})} \rightarrow \text{NH}_2\text{CHO}_{(\text{g})} + \text{H}_{(\text{g})}$ from the network. The rationale for excluding this reaction follows the finding by Song & Kästner (2016) that the entrance barrier to the reaction is too high to be viable, although Barone et al. (2015) suggest the converse. The fact that formamide remains overproduced in our models, in spite of the absence of this reaction, implies that the efficiency of our Reaction (13) is too high, as it is the only major formation pathway in the network. It is possible that the $\text{NH}_{2(\text{s})}$ and $\text{HCO}_{(\text{s})}$ radicals are segregated within actual ices. Given the high extinction threshold of CO (Whittet et al. 2001), $\text{HCO}_{(\text{s})}$ could be expected to occupy outer ice layers to a greater extent than $\text{NH}_{2(\text{s})}$, a possibility that our models cannot explicitly take into account in their subsequent chemistry. However, the collapse stage of our models does indeed allow the layering of these species to be traced during the formation of the ice on the grain surfaces and indicates that the radicals NH_2 and HCO both share their highest cumulative abundances with respect to water in outer ice layers (Figure 14). An alternative explanation is that the reaction of $\text{NH}_{2(\text{s})}$ and $\text{HCO}_{(\text{s})}$, which has another product branch, to form ammonia and $\text{CO}_{(\text{s})}$, may not have the appropriate branching ratios, which are currently assumed to be 1:1. Indeed, H abstraction by $\text{NH}_{2(\text{s})}$ should be efficient, and this branch may be underestimated in the models.

5.4. Implications for Glycine Detection

According to model results, glycine achieves the largest peak solid- and gas-phase abundances for models with medium t_{wu}

Table 7
Calculated Column Densities for Glycine Using Best-fit Models for Each Source

Source	$N_{\text{tot}} \text{ (cm}^{-2}\text{)}$
NGC 6334 IRS 1	1.3(15)
NGC 7538 IRS 1	8.2(12)
W3(H_2O)	4.0(14)
W33A	6.4(13)

and large ζ (Figure 4, panel $t_5\zeta_9$), corresponding to $t = 5.00 \times 10^4$ yr and $\zeta = 8.32 \times 10^{-16} \text{ s}^{-1}$. From these results, we may assert that larger ζ are most conducive to glycine formation. In the efforts to detect glycine, we may consider sources with similar ionization rates. For example, van der Tak et al. (2006) calculate $\zeta = 4 \times 10^{-16} \text{ s}^{-1}$ toward Sgr B2, which is consistent for producing glycine in large abundances in our models.

The best-fit models may also offer an indication of glycine abundances in the four sources surveyed. We cite values of N_{tot} for glycine using the best-fit models in Table 7. NGC 6334 IRS 1 and W3(H_2O) have the largest N_{tot} of $1.3 \times 10^{15} \text{ cm}^{-2}$ and $4.0 \times 10^{14} \text{ cm}^{-2}$ respectively. Accordingly, these sources may be also be candidates for future efforts to detect glycine with ALMA.

6. Conclusions

In this study, we have investigated the effects of varying the cosmic-ray ionization rate and warm-up timescale on the chemistry of COMs in hot cores. Clear behaviors emerge from this treatment, and trends may be identified in the interplay between the two physical parameters tested. However, it is also clear from this work that degeneracy between the two is limited; the total fluence of cosmic rays in these models is important, but the observable abundances of COMs depend on the explicit values of both the cosmic-ray ionization rate and the period of exposure.

By mapping the generic models onto physical profiles from the literature for observed sources, we have identified the best-fit model to reproduce observed molecular line emission from each of four hot-core sources. Although this method is simple, it has turned out to be a powerful technique and has produced clear relationships between the best-fit cosmic-ray ionization rate and warm-up timescale and the physical characteristics of the observed sources. The fact that these relationships exist and are well behaved—especially that between the warm-up timescale and the hot-core mass—indicates that the determination of the best-fit models is meaningful. The fits to observed sources and the relationships between physical quantities that they establish may be useful for adaptation to modeling other hot-core sources. More dynamically detailed chemical simulations of both specific observational sources and generic, model sources would be valuable to improve the constraint of the key physical quantities.

The use of COM abundances in this way to constrain cosmic-ray ionization rates naturally tends to bias those ionization rates toward those most appropriate for the dense regions in which such molecules are found. This is an improvement over more direct observational/modeling techniques that are based on ion abundances in more diffuse regions. The relationship between cosmic-ray ionization rate and total hydrogen column density that is established in the present

study is consistent with values at the upper limit of, or somewhat higher than, those established by others through separate theoretical calculations (Padovani et al. 2018).

Here we list a selection of main conclusions from this study:

1. The grid of chemical models of various cosmic-ray ionization rates and warm-up timescales indicates that larger ζ values tend to produce more radicals in the dust-grain-surface ices, which can react to form large abundances of COMs; at the highest ζ values tested here, destruction of these COMs on grains at higher temperatures and in the gas phase is also widespread.
2. These destructive effects associated with cosmic rays are most pronounced for long warm-up timescales (t_{wu}). The trends suggest that sources with intermediate warm-up timescales that also have medium to large ζ values (10^{-16} s^{-1}) may be the most chemically rich.
3. The direct comparison between observed and modeled emission-line-integrated intensities has proved to be a useful method for testing the fidelity of the models to observational COM abundances, which removes the requirement to obtain unique column density and excitation temperature values for each molecule.
4. The best-fitting models for four observed hot-core sources all provide cosmic-ray ionization rates higher than the canonical value and warm-up timescales shorter than any values previously used in our models.
5. The best-fitting models demonstrate a strong negative correlation ($r = -0.87$) between ζ and total hydrogen column density for each source. An even stronger negative correlation ($r = -0.97$) is found between warm-up timescale and total source mass, based on the integrated density profile. The emergence of these relationships gives further confidence in the validity of the chemical model fits. Assuming that density profiles for a specific source exist, these relationships may be useful in determining cosmic-ray ionization rates and warm-up timescales for other sources, in the absence of other information.
6. Following the chemical trends, glycine is produced in its largest abundance for medium t_{wu} and large ζ . Accordingly, observational efforts to detect it may benefit from studying sources with ζ on the order of 10^{-16} s^{-1} that also have only a modest total mass (to provide a longer warm-up timescale). NGC 6334 IRS 1 and W3(H₂O) also have the largest calculated values of N_{tot} , so they may be good targets for future detection.
7. Our models fail to reproduce observed results for formaldehyde, formic acid, and formamide. These molecules are generally overproduced by around two orders of magnitude. This could be attributed to problems with branching ratios of formation reactions that are present in the chemical network, to problems with trapping species in the ice, and to the use of a purely LTE radiative transfer model.
8. The best fits to modeled integrated intensities for W3(H₂O) lie in different regions of the cosmic-ray fluence grid, as some molecules agree well in one region, whereas others agree in a different region. The behavior could be attributed to the fact that the source is a protobinary system. If this is true, then it would imply that the existence of source substructure can be inferred

through modeling t_{wu} and ζ , if those values differ between substructures.

9. NGC 6334 IRS 1 and W3(H₂O) have the best agreement among modeled and observed integrated intensities, whereas NGC 7538 IRS 1 and W33A have the worst. Poor mapping of static warm-up models to the temperature and density profiles may contribute to poor agreement.

We wish to thank the referees for their helpful comments and suggestions for preparing this manuscript. This work is partially funded by a grant from the NASA Astrophysics Theory Program, grant No. 80NSSC18K0558.

ORCID iDs

Christopher J. Barger  <https://orcid.org/0000-0002-6874-3404>

Robin T. Garrod  <https://orcid.org/0000-0001-7723-8955>

References

- Allen, M., & Robinson, G. W. 1977, *ApJ*, **212**, 396
- Allen, V., van der Tak, F. F. S., & Walsh, C. 2018, *A&A*, **616**, A67
- Álvarez-Barcia, S., Russ, P., Kästner, J., & Lamberts, T. 2018, *MNRAS*, **479**, 2007
- Alvarez-Idaboy, J. R., Mora-Diez, N., Boyd, R. J., & Vivier-Bunge, A. 2001, *J. Am. Chem. Soc.*, **123**, 2018
- Barone, V., Latouche, C., Skouteris, D., et al. 2015, *MNRAS*, **453**, L31
- Belloche, A., Garrod, R. T., Müller, H. S. P., & Menten, K. M. 2014, *Sci*, **345**, 1584
- Belloche, A., Garrod, R. T., Müller, H. S. P., et al. 2009, *A&A*, **499**, 215
- Belloche, A., Meshcheryakov, A. A., Garrod, R. T., et al. 2017, *A&A*, **601**, A49
- Beuther, H., Linz, H., & Henning, T. 2013, *A&A*, **558**, A81
- Bisschop, S. E., Jørgensen, J. K., van Dishoeck, E. F., & de Wachter, E. B. M. 2007, *A&A*, **465**, 913
- Brogan, C. L., Hunter, T. R., Cyganowski, C. J., et al. 2018, *ApJ*, **866**, 87
- Butscher, T., Duvernay, F., Danger, G., & Chiavassa, T. 2016, *A&A*, **593**, A60
- Caproni, A., Abraham, Z., & Vilas-Boas, J. W. S. 2002, IAU Symp. 206, Cosmic Masers: From Proto-Stars to Black Holes (San Francisco, CA: ASP), 240
- Caselli, P., Walmsley, C. M., Terzieva, A., & Herbst, E. 1998, *ApJ*, **499**, 234
- Ceccarelli, C., Hily-Blant, P., Montmerle, T., et al. 2011, *ApJL*, **740**, L4
- Charnley, S. B., Tielens, A. G. G. M., & Millar, T. J. 1992, *ApJL*, **399**, L71
- Chen, H. R., Welch, W. J., Wilner, D. J., & Sutton, E. C. 2006, *ApJ*, **639**, 975
- Choudhury, R., Schilke, P., Stephan, G., et al. 2015, *A&A*, **575**, A68
- DeMore, W. B., Sander, S. P., Golden, D. M., et al. 1997, Jet Propulsion Laboratory Publication, 97-4, 1
- Duley, W. W., & Williams, D. A. 1993, *MNRAS*, **260**, 37
- Favre, C., Ceccarelli, C., López-Sepulcre, A., et al. 2018, *ApJ*, **859**, 136
- Gaches, B. A. L., Offner, S. S. R., & Bisbas, T. G. 2019, *ApJ*, **878**, 105
- Garrod, R. T. 2008, *A&A*, **491**, 239
- Garrod, R. T. 2013, *ApJ*, **765**, 60
- Garrod, R. T., & Herbst, E. 2006, *A&A*, **457**, 927
- Garrod, R. T., & Pauly, T. 2011, *ApJ*, **735**, 15
- Garrod, R. T., Wakelam, V., & Herbst, E. 2007, *A&A*, **467**, 1103
- Garrod, R. T., & Widicus Weaver, S. L. 2013, *ChRv*, **113**, 8939
- Garrod, R. T., Widicus Weaver, S. L., & Herbst, E. 2008, *ApJ*, **682**, 283
- Geppert, W. D., Hamberg, M., Thomas, R. D., et al. 2006, *FaDi*, **133**, 177
- Goldsmith, P. F., & Langer, W. D. 1999, *ApJ*, **517**, 209
- Hamberg, M., Österdahl, F., Thomas, R. D., et al. 2010, *A&A*, **514**, A83
- Hasegawa, T. I., & Herbst, E. 1993, *MNRAS*, **263**, 589
- Herbst, E., & Millar, T. J. 2008, in The Chemistry of Cold Interstellar Cloud Cores, ed. I. W. M. Smith (London: Imperial College Press), 1
- Herbst, E., & van Dishoeck, E. F. 2009, *ARA&A*, **47**, 427
- Hidaka, H., Watanabe, N., Shiraki, T., Nagaoka, A., & Kouchi, A. 2004, *ApJ*, **614**, 1124
- Ivlev, A. V., Padovani, M., Galli, D., & Caselli, P. 2015, *ApJ*, **812**, 135
- Izquierdo, A. F., Galvan-Madrid, R., Maud, L. T., et al. 2018, *MNRAS*, **478**, 2505

- Kalván, J. 2018, IAU Symp. 332, *Astrochemistry VII: Through the Cosmos from Galaxies to Planets* (Cambridge: Cambridge Univ. Press), 374
- Le Petit, F., Roueff, E., & Herbst, E. 2004, *A&A*, 417, 993
- Le Petit, F., Ruaud, M., Bron, E., et al. 2016, *A&A*, 585, A105
- Molinari, S., Brand, J., Cesaroni, R., & Palla, F. 2000, *A&A*, 355, 617
- Öberg, K. I., Garrod, R. T., van Dishoeck, E. F., & Linnartz, H. 2009a, *A&A*, 504, 891
- Öberg, K. I., van Dishoeck, E. F., & Linnartz, H. 2009b, *A&A*, 496, 281
- Öberg, K. I., van Dishoeck, E. F., & Linnartz, H. 2009c, *ApJ*, 693, 1209
- Ocaña, A. J., Jiménez, E., Canosa, A., et al. 2017, *ApJ*, 850, 28
- Oka, T., Geballe, T. R., Goto, M., Usuda, T., & McCall, B. J. 2005, *ApJ*, 632, 882
- Padovani, M., & Galli, D. 2011, *A&A*, 530, A109
- Padovani, M., Galli, D., Ivlev, A. V., et al. 2018, *A&A*, 614, A144
- Padovani, M., Walmsley, C. M., Tafalla, M., et al. 2009, *A&A*, 505, 1199
- Prasad, S. S., & Tarafdar, S. P. 1983, *ApJ*, 267, 603
- Rimmer, P. B., Herbst, E., Morata, O., & Roueff, E. 2012, *A&A*, 537, A7
- Rimola, A., Taquet, V., Ugliengo, P., et al. 2014, *A&A*, 572, A70
- Shingledecker, C. N., Le Gal, R., & Herbst, E. 2017, *Phys. Chem. Chem. Phys.*, 19, 11043
- Shingledecker, C. N., Tennis, J. D., Le Gal, R., & Herbst, E. 2018, *ApJ*, 861, 1
- Snyder, L. E., Lovas, F. J., Hollis, J. M., et al. 2005, *ApJ*, 619, 914
- Song, L., & Kästner, J. 2016, *Phys. Chem. Chem. Phys.*, 18, 29278
- Taquet, V., Wiström, E. S., & Charnley, S. B. 2016, *ApJ*, 821, 46
- Tideswell, D. M., Fuller, G. A., Millar, T. J., & Marwick, A. J. 2010, *A&A*, 510, A85
- van der Tak, F. F. S., Belloche, A., Schilke, P., et al. 2006, *A&A*, 454, L99
- van der Tak, F. F. S., & van Dishoeck, E. F. 2000, *A&A*, 358, L79
- van der Tak, F. F. S., van Dishoeck, E. F., Evans, N. J., II, & Blake, G. A. 2000, *ApJ*, 537, 283
- Vaupré, S., Hily-Blant, P., Ceccarelli, C., et al. 2014, *A&A*, 568, A50
- Viti, S., Collings, M. P., Dever, J. W., McCoustra, M. R. S., & Williams, D. A. 2004, *MNRAS*, 354, 1141
- Viti, S., & Williams, D. A. 1999, *MNRAS*, 354, 1141
- Watanabe, N., & Kouchi, A. 2002, *ApJL*, 571, L173
- Webber, W. R. 1998, *ApJ*, 506, 329
- Whittet, D. C. B., Gerakines, P. A., Hough, J. H., & Shenoy, S. S. 2001, *ApJ*, 547, 872
- Yetter, R. A., Rabitz, H., Dryer, F. L., et al. 1989, *JChPh*, 91, 4088
- Yusef-Zadeh, F., Hewitt, J. W., Wardle, M., et al. 2013, *ApJ*, 762, 33
- Zanchet, Z., del Mazo, P., Aguado, A., et al. 2018, *Phys. Chem. Chem. Phys.*, 20, 5415